國立臺灣科技大學
電 機 工 程 系

碩士學位論文

學　號: M9607236

基於曲折繞接線變壓器利用特定諧波消除之多階層反流器研製

Implementation of a Multi-level Inverter Based on Zig-zag Connected Transformers Using Selective Harmonic Elimination

研 究 生：劉彥中
指導教授：楊宗銘 博士

中華民國 九十八年七月一日

碩士學位論文指導教授推薦書

指導教授：楊宗銘

本校　電機工程系　　劉彥中　君

所提之論文：

基於曲折繞接線變壓器利用特定諧波消除之多階層反流器研製

係由本人指導撰述，同意提付審查。

指導教授 楊宗銘

98 年 7 月 1 日

碩士學位考試委員審定書

M9607236

指導教授：楊宗銘

本校　電機工程系　　劉彥中　君

所提之論文：

基於曲折繞接線變壓器利用特定諧波消除之多階層反流器研製

經本委員會審定通過，特此證明。

學校考試委員會

委　　員：

指導教授：楊宗銘

學程主任：

系主任（所長）：

中華民國 98 年 7 月 1 日

摘要

本文應用選擇諧波消除(selective harmonic elimination)技術計算一反流器系統之開關切換角度，此反流器系統配合曲折繞接式(zig-zag)變壓器於輸出端。不同於選擇諧波消除技術常用的四分之一波對稱之波形，本文之脈波寬度調變波形使用半波對稱波形。儘管使用半波對稱波形在計算上較繁雜，但可提供較多的解並有機會得到較好的解。由於選擇諧波消除技術可直接控制特定諧波，因此適用於對特定諧波有抑制能力的設備如曲折繞接式變壓器。本文提出的系統中，兩組變壓器的一次側電壓由兩組六開關之全橋反流器供應，且此兩組反流器之電壓波形有 30 度之相位差。此變壓器可將 $12n\pm1$ 次以外的諧波抑制在變壓器二次側，因此半波對稱的選擇諧波消除方法設計消除 $12n\pm1$ 次的諧波成份與控制基本波的大小。根據上述規範，本文建立一小型系統來驗證其可行性。

關鍵詞： 選擇諧波消除、 曲折繞接式變壓器

Abstract

This thesis applies the selective harmonic elimination (SHE) technique to determine the switching angles for an inverter system that is cooperated with special connected transformers called zig-zag connected transformers. Unlike quarter-wave symmetry, most employed in SHE strategy, half-wave symmetry is used in this thesis. Although half-wave symmetry needs more calculation burdens than quarter-wave symmetry, it provides wider solution space and better solutions. Attributed to directly controlling harmonics, SHE technique has the adaptability to associate with apparatus which are congenitally immune to specific harmonics, such as the zig-zag connection transformers. In this thesis, two sets primary windings of the transformers are supplied by two 6-switch full-bridge inverters with 30 electrical degrees phase shift. Prohibited by the transformers, harmonics with orders other than $12n \pm 1$ (n is positive integral number) will not appear in the line-to-line voltage of the secondary side. Then, SHE technique with half-wave symmetry is employed to handle harmonics with orders equal to $12n \pm 1$, and controls the amplitude of the fundamental. Based on specifications described above, a small-size prototype is built to verify the practical validity of the proposed system.

Keywords: Selective harmonic elimination, zig-zag connection.

Acknowledgements

首先感謝楊宗銘教授在這兩年的悉心指導與教誨，老師嚴謹的治學態度，理論與實務並重的訓練和高度的執行力讓T2-402實驗室日漸茁壯，也讓我學習到研究的方法和做事的態度。這篇論文在老師的指導和細心的編修中得以趨近完善。

實驗室的學長學弟們各有所長，在與他們的切磋討論下許多問題都可迎刃而解。感謝巫昇峰學長，本篇論文以他的研究為基石，研究中他也給予很多建議，感謝寶勝、軒宇、奕翰、彥寧、建祥、青龍、綜毅、乃文、志勝、宜勳、良弘學長和銘輝學長，在課業與研究上一起學習、討論及成長。在忙碌之餘，陪我打球、出遊及談心，讓我的研究生生活更豐富多彩。

最後感謝我的母親，哥哥與姊姊在背後默默的支持，我會朝著理想繼續努力下去。

Table of Contents

List of Figures

List of Tables

Chapter1 Introduction

1.1 Background and motivation

With the flourish of the high-tech industry, equipment and facilities need higher power with higher quality. When equipment is directly powered by power plant, the power quality is uncontrollable, which sometimes harms the performance of the equipment. The development of dc-to-ac inverter can deal with this problem. Switching-mode dc-to-ac inverters are used in ac motor drives and uninterruptible ac power supplies. The voltage source inverters (VSIs) can be further divided into some general categories [1], such as sinusoidal pulse-width-modulated (SPWM) inverters [2-5], square-wave inverters [6-7] and single-phase inverters with voltage cancellation. The first kind requires higher switching frequency, and the rest two kinds have bigger harmonic distortion. The technique of selective harmonic elimination (SHE) has been developed for more than forty years [8] and has been applied to many inverter systems. The primary advantages of SHE include providing lower switching frequency, directly controlling harmonic components, and optimizing particular objects [9-11]. Thus SHE is a popular choice among different methods of modulation in many static power conversion applications.

Depending on the applications, such as the topology of inverters and the number of phase, there are many perspectives can be used to formulate the SHE problems. After the problem is formulated, a set of nonlinear equations, traditionally generated from Fourier series representation and the optimizing objective function both based on the

specific perspective, has to be solved before obtaining the desired switching angles. It is well known that on-line solving these nonlinear equations [12-15] has been an obstacle to engineers who are trying to apply SHE technique to their systems. Moreover, once the number of variables in the nonlinear equations increases, the burden of calculating also increases significantly. Thus, most SHE applications use off-line calculation to ease the complication of the system. In order to reduce the memory size of the micro-controller, this thesis calculates the switching angles on-line by piece-wise continuous polynomials representing the off-line calculated solutions [16]. This method is verified in practical verification in this thesis. To reduce the number of variables, the output waveforms are always constrained to be symmetric. For example, by making half-wave symmetry assumption to SHE formulations, even harmonics are eliminated automatically. Furthermore, quarter-wave-symmetry assumption, which imposes more constraints but requires lesser variables, is more popular than half-wave-symmetry assumption [17-20]. With quarter-wave-symmetry assumption, all harmonics have either 0 or 180 degrees phase shift with respect to the fundamental, while half-wave-symmetry assumption allows harmonic phasing to vary. Although the former is convenient for solving the nonlinear equations, it often results in sub-optimal solutions.

1.2 Objectives of the thesis

Attributed to directly controlling harmonics in the output waveform, SHE techniques have the adaptability to associate with apparatus which are congenitally immune to specific harmonics, such as the zig-zag connected transformers [21-22]. When SHE associates with such electric apparatus, the strategy of SHE can leave those specific harmonics uncontrolled or maximize them and focus efforts on harmonics which are most concerned. According to this strategy, either the lowest switching frequency or output distortion can be achieved.

In some dc/ac applications, the output transformers are deployed to adjust the voltage level between primary and secondary sides and/or to meet the isolation requirement. For example, the static inverter (SIV), which provides ac power for air conditioning and lighting on electric trains in Taiwan, deploys two three-phase transformers with zig-zag connection in their secondary windings. This structure will be illustrated in next chapter. It can be shown that, with this kind of connection, harmonics with orders other than $12n \pm 1$ present in the primary windings will be trapped in the secondary windings and absent in the line-to-line voltages of the secondary side.

In this thesis, SHE technique with half-wave-symmetry assumption is investigated to obtain the switching angles for an inverter system that deploys two zig-zag connection transformers in output stage [23]. The two sets of primary windings of the transformers are supplied by two 6-switch full-bridge inverters with 30 electrical degrees phase shift. As mentioned above, harmonics with orders other than $12n \pm 1$ will not

appear in the line-to-line voltage in the secondary side. Thus, SHE technique with half-wave symmetry is employed to handle harmonics with orders equal to $12n \pm 1$, and control the amplitude of the fundamental. The uncontrolled harmonic profiles of the output waveform obtained under half-wave-symmetry assumption are different from those with quarter-wave-symmetry assumption. In other words, it is possible that the former provides better solutions than the latter in this application. Based on the strategy that the fundamental is controllable and 11th and 13th harmonics are eliminated, a set of full-range (both amplitude and phase of the fundamental) solutions with three switching angles are obtained. By the help of the transformers, we can choose the switching angles with minimum 23-rd and 25-th harmonics, which are the most concerned in this thesis. Some selected analysis and experimental results are shown in this thesis.

For voltage compensation, the selected solutions of each fundamental can be calculated by interpolation method using established look-up table in the microcontroller. Therefore, this approach needs huge memory size. It's a better way to transform the huge amount of data into polynomials by the least-squares method [24]. We exploit second-order-piecewise-continuous polynomials to approximate the practical data in order to reduce the error caused by the deviation between the exact solutions and the solutions derived by non-piecewise approximated polynomials. However, more segments causes more memory consumption. There is a dilemma between the precision required and the memory size needed. In this thesis, the primary side of the zig-zag transformer is connected to two sets of two-level inverter. A three

-phase L-C filter is connected to the output side of the zig-zag transformer for further THD reduction. A small-size prototype is built to verify the practical validity of the proposed system.

1.3 Organization of the thesis

The following states the organization of this thesis.

Chapter1: This chapter investigates the background of inverter switching strategy and the motivation of this thesis. The objective of this thesis is illustrated in this chapter as well.

Chapter2: Inverter and zig-zag transformers are the most important parts of this system. This chapter illustrates the principals and detailed mathematical analyses.

Chapter3: This thesis adopts selective harmonic elimination as the switching strategy of the inverter, offering both theoretical and mathematical analysis in this chapter. The approximated polynomials representing the optimized solutions are found to realize the on-line calculation.

Chapter4: This chapter offers detailed hardware and software structure of the proposed system and the specifications of each component, illustrating the DSP deployment and the software programming.

Chapter5: This chapter shows the simulation and experimental results.

Chapter6: The conclusion of this thesis.

Chapter 2 Inverters and zig-zag connected transformers

2.1 Introduction

Figure 2-1 shows the diagram of the proposed system including two 6-switch full-bridge inverters, two transformers, a DSP-based controller and an L-C filter connected to the output side. The two transformers are individually supplied by two 6-switch full-bridge inverters [24], denoted as INV1 and INV2, which receive switching signals from the digital controller. Two sets of inverters convert the DC voltage from the DC source into two sets of three-phase PWM waveforms, which have 30-degree phase difference, with harmonics controlled. Ascribed to the zig-zag connection of the secondary windings, some characteristic harmonics are prevented from appearing in the output line-to-line voltage. The output voltage of the filter is then detected for voltage compensation by a voltage-sensor circuit in which a rectifier model is involved. In this chapter, we are going to dwell on the structure and the operation of the three-phase full-bridge inverters. This chapter also analyses the zig-zag transformers in detail.

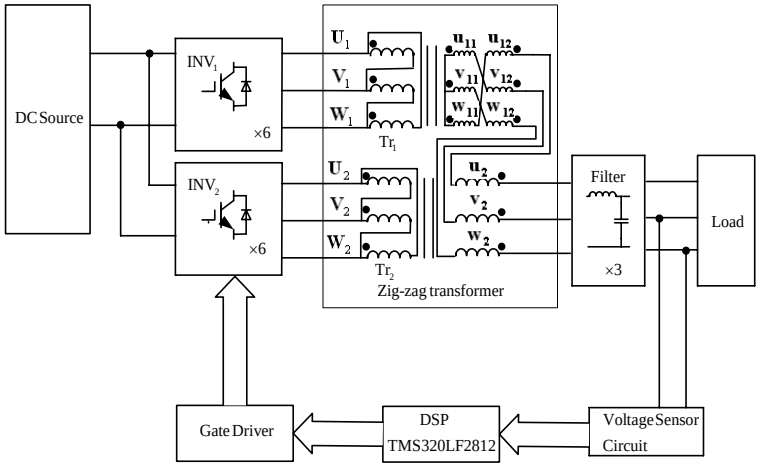

Fig. 2-1 The diagram of the proposed system.

2.2 The three-phase inverter

Fig. 2-2 shows two two-level full-bridge inverters powered by one dc source in parallel with six switches in each set. Each leg of the three-phase inverters is constructed by two switches in series. It should be noted that synchronously turning on the switches in the same leg will rapidly ruin the switch. Each leg of inverters rules one phase of waveform feeding the transformers. The output waveforms $\mathbf{U}_1$, $\mathbf{V}_1$ and $\mathbf{W}_1$ are synchronous to the trigger signals SU_1, SV_1 and SW_1, and the output waveforms $\mathbf{U}_2$, $\mathbf{V}_2$ and $\mathbf{W}_2$ are also identical to the trigger signals of SU_2, SV_2 and SW_2.

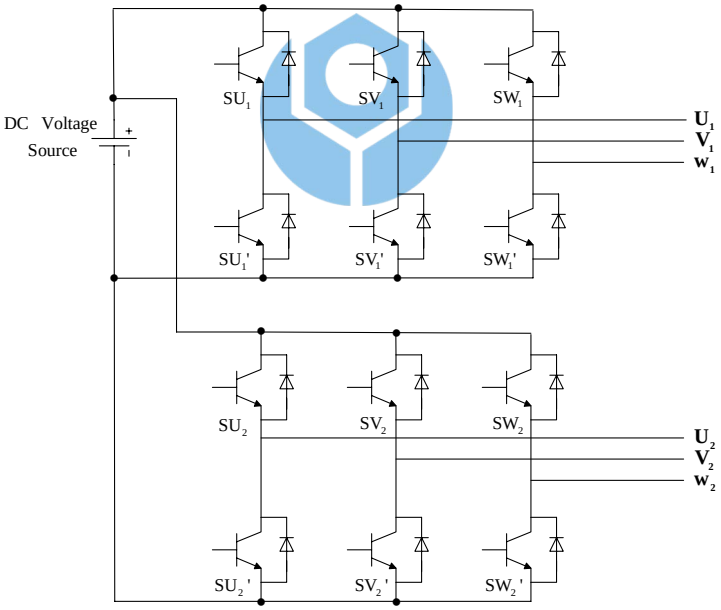

Fig. 2-2 Full-bridge inverter diagram.

To match the criteria of the transformer inputs, the output waveforms of $\mathbf{U}_1$, $\mathbf{V}_1$ and $\mathbf{W}_1$ are three-phase balanced. The other three-phase output waveforms $\mathbf{U}_2$, $\mathbf{V}_2$ and $\mathbf{W}_2$ are lagged 30 degrees behind $\mathbf{U}_1$, $\mathbf{V}_1$

and $\mathbf{W}_1$. Fig. 2-3 shows the triggered signals for switches in INV1, where the voltage level depends on the dc power applied to the driver circuits. Fig. 2-4 shows the output line-to-line voltages of INV1 powered by 20-Volt dc bus. The triggered signals of INV2 are lagged 30 degrees behind the triggered signals of INV1, the output line-to-line voltages of INV2 are lagged 30 degrees behind the line-to-line voltages of INV1 as well.

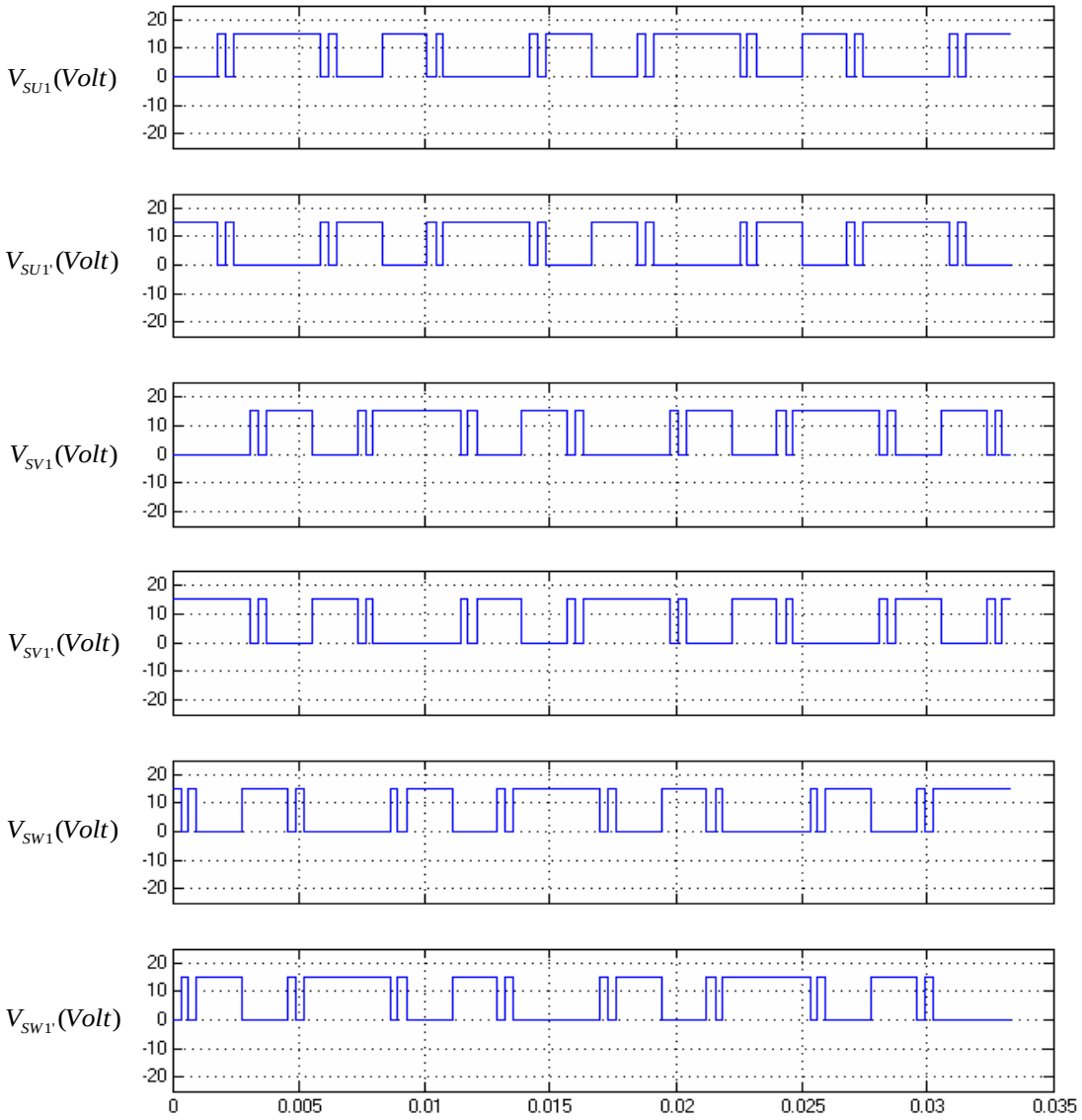

Fig. 2-3 The triggering signals of switches in INV1.

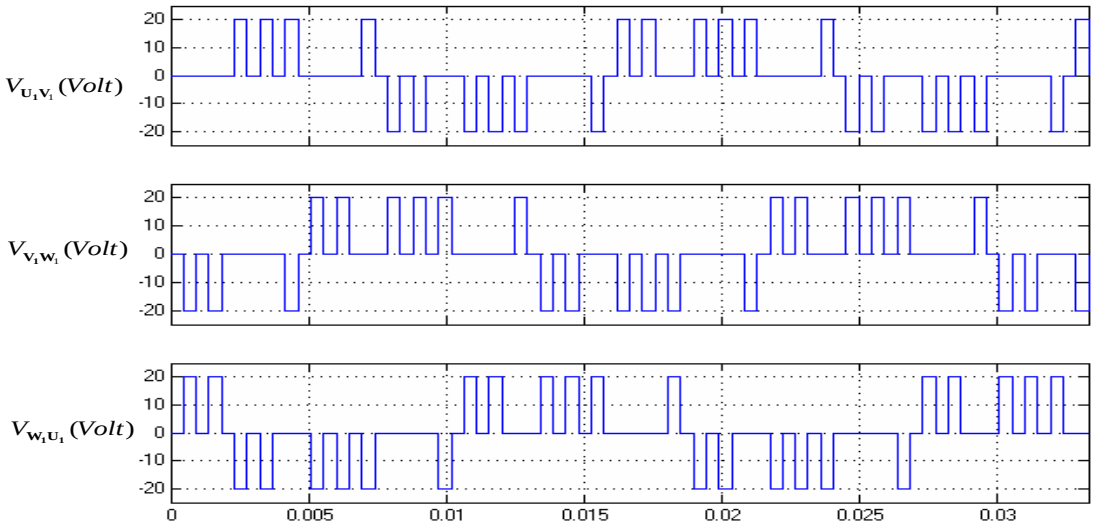

Fig. 2-4 The output line-to-line voltage of INV1 with a dc bus of 20 *Volt*.

2.3 Analysis of the zig-zag connected transformers

Fig. 2-5 shows the diagram of the zig-zag connected transformers including two transformers denoted as Tr1 and Tr2. It have delta connections in the primary sides, while the secondary windings of the Tr1, which has two identical windings in each phase, employ interconnection and then are in series with the secondary windings of Tr2. The turn ratio between secondary windings of Tr1 and Tr2 is $1:\sqrt{3}$ and the turn ratio between primary and secondary is dependent on voltage levels of both sides. This special connection of the secondary windings of the transformers provides immunity from some harmonics. Before taking this advantage, an assumption has to make first, that is, these two transformers have to be supplied by two phase-shifted ac sources with 30 electrical degrees.

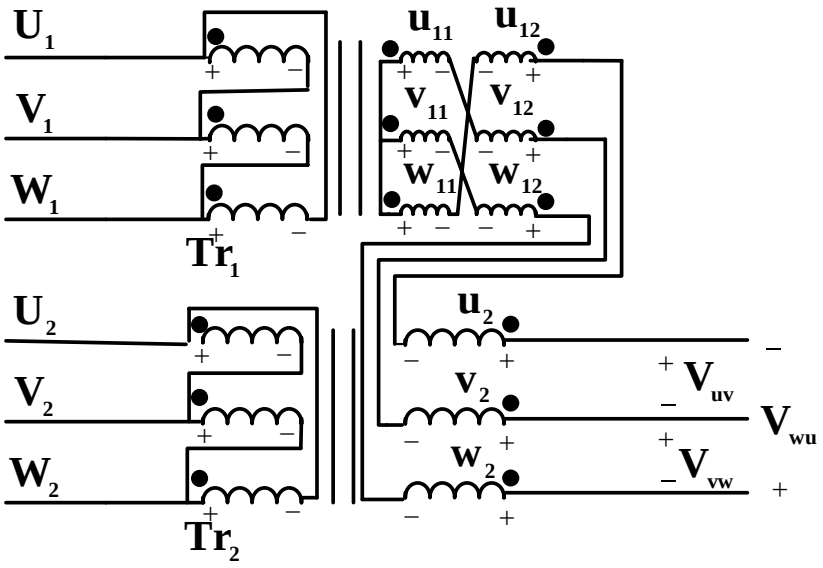

Fig. 2-5 The zig-zag transformers diagram.

Under this assumption, Fig. 2-6 shows the phasor diagram of the fundamental voltages of the transformers. $\mathbf{U}_x$, $\mathbf{V}_x$ and $\mathbf{W}_x$, where $x=1$ and 2, are denoted as the primary voltage phasors of Tr1 and Tr2 respectively, and $\mathbf{u}_{11}$, $\mathbf{v}_{11}$, $\mathbf{w}_{11}$, $\mathbf{u}_{12}$, $\mathbf{v}_{12}$, $\mathbf{w}_{12}$, $\mathbf{u}_2$, $\mathbf{v}_2$, $\mathbf{w}_2$ are denoted as the secondary voltage phasors of Tr1 and Tr2 respectively. It can be seen that the output side (secondary side) is basically in Y-connection and each phase is composed of three phasors. Thus, the output line-to-line voltages can be expressed as

$$\mathbf{V}_{uv}=\mathbf{u}_2+\mathbf{u}_{12}-\mathbf{w}_{11}+\mathbf{u}_{11}-\mathbf{v}_{12}-\mathbf{v}_2 \quad (2\text{-}1)$$

$$\mathbf{V}_{vw}=\mathbf{v}_2+\mathbf{v}_{12}-\mathbf{u}_{11}+\mathbf{v}_{11}-\mathbf{w}_{12}-\mathbf{w}_2 \quad (2\text{-}2)$$

$$\mathbf{V}_{wu}=\mathbf{w}_2+\mathbf{w}_{12}-\mathbf{v}_{11}+\mathbf{w}_{11}-\mathbf{u}_{12}-\mathbf{u}_2 \quad (2\text{-}3)$$

where $\mathbf{V}_{uv}$, $\mathbf{V}_{vw}$ and $\mathbf{V}_{wu}$ are phasors of the output line-to-line voltages.

The two-level PWM inputs will be added up to 9-level output line-to-line

voltages with harmonics eliminated.

As shown in Fig. 2-1, through proper time delay, it is easy for the digital controller to generate switching signals that trig the inverters' switches and then provides two balanced three-phase ac sources with 30 degrees phase shift between their fundamentals of the outputs of INV1 and INV2 in spite of the pulse-width-modulation (PWM) methods. In most case, the output waveforms of the inverters contain fundamental and several harmonic components as well, that means the fundamental of $\mathbf{U}_1$ is leading (or lagging) the fundamental of $\mathbf{U}_2$ by 30 degrees, while the h-th harmonic of $\mathbf{U}_1$ is leading (or lagging) the harmonic of $\mathbf{U}_2$ by $30\times h$ degrees. The proposal switching signals, which are determined by SHE technique with half-wave-symmetry assumption, will be detailed later in next chapter.

Eq. (2-1) - Eq. (2-3) are not only useful to determine the fundamentals in the line-to-line voltages, but also available to determine the harmonics, except that different order of harmonic has different phase angle. By calculating Eq. (2-1) - Eq. (2-3), it can be proved that harmonics with orders other than $12n\pm 1$ will not appear in the line-to-line voltage in the secondary side. Table 1-1 shows calculating results from Eq. (2-1) for harmonics with and without orders of $12n\pm 1$. For convenience, u_{11} is selected as the reference phasor with unit amplitude and zero-phase angle for each harmonic component. The harmonics with orders 3+12m, where $m=0,\ 1,\ 2,...$ have the same phasor representations of the six phasors

in Eq. (2-1) to determine $\mathbf{V}_{uv}$, and the results of $\mathbf{V}_{uv}$ are all zeros. Moreover, the harmonics with orders $k+12m$, where $k=3,\ 5,\ 7$ and 9, have similar formalizations. Nevertheless, the harmonics with orders 11+12m and 13+12m, i.e. $12n\pm1$, have non-zero $\mathbf{V}_{uv}$. As all odd-order harmonics are considered in Table 1-1, it can conclude from above that harmonics with orders other than $12n\pm1$ present in the primary windings will be trapped in the secondary windings and absent in the line-to-line voltages of the secondary side. Identical results of calculating $\mathbf{V}_{vw}$ and $\mathbf{V}_{wu}$ can be obtained from Eq. (2-2) and (2-3) respectively.

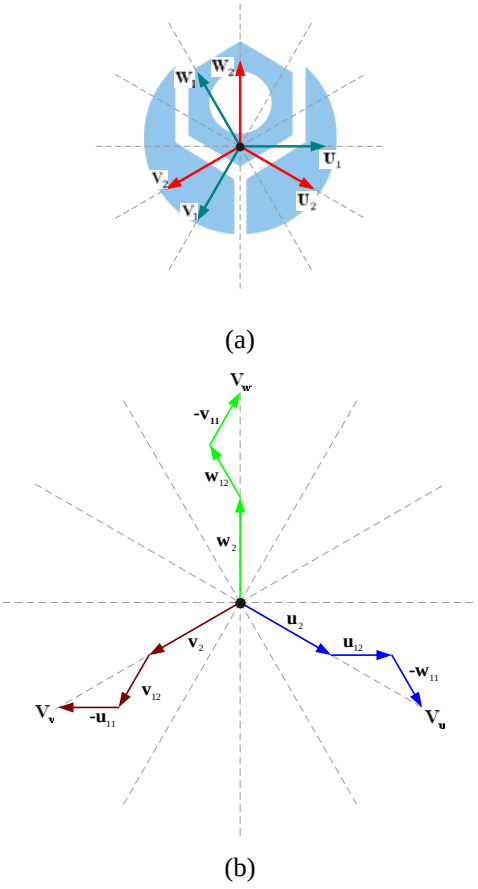

Fig. 2-6 Fundamental phasor diagram of zig-zag transformers, (a) primary, (b) synthesize of secondary.

Table 1-1 Calculating $\mathbf{V}_{uv}$ with respect to different harmonics.

Order of harmonic	$\mathbf{u}_2$	$\mathbf{u}_{12}$	$\mathbf{w}_{11}$	$\mathbf{u}_{11}$	$\mathbf{v}_{12}$	$\mathbf{v}_2$	$\mathbf{V}_{uv}$
1	1.5-j0.866	1	-0.866+j1.5	1	-0.866-j1.5	-1.5-j0.866	6.735
3+12m	-j1.733	1	-1	1	-1	j1.733	0
5+12m	-1.5-j0.866	1	0.5+j0.866	1	0.5-j0.866	-1.5+j0.866	0
7+12m	-1.5+j0.866	1	0.5-j0.866	1	0.5+j0.866	-1.5-j0.866	0
9+12m	j1.733	1	-1	1	-1	-j1.733	0
11+12m	1.5+j0.866	1	-0.5-j0.866	1	-0.5+j0.866	-1.5+j0.866	5.997
13+12m	1.5-j0.866	1	-0.5+j0.866	1	-0.5-j0.866	-1.5-j0.866	5.997

Chapter3 Selective harmonic elimination strategy

3.1 Introduction

According to the discussion in chapter 2, the output line-to-line voltages of zig-zag connected transformers exist large amount of 11-th and 13-th harmonics that can not be prohibited by the transformers. In this chapter, we are going to deal with these two harmonic components by selective harmonic elimination method. The next two harmonics which can not be prohibited by the transformer are 23-rd and 25-th harmonics. These two harmonics can be suppressed by suitable shifting the phase of the fundamental, meanwhile the quarter-wave-symmetric constraint on the designed waveform changes into half-wave symmetry. Consequently, the total harmonic distortion can be reduced by this method without increasing switching frequency. However, when the designed waveform with half-wave symmetry is considered, the calculation burden and difficulty increase as well. Newton-Rephson [25-27] method is chosen to solve the non-linear equation set derived from SHE method, and some selected solutions of both quarter-wave and half-wave symmetry constraint problems are obtained.

3.2 The Theory of Fourier series expansion

The Fourier series divide periodical signal into sinusoidal waveforms with different magnitudes and different orders of frequency. In general, a periodical waveform $f(t)$ can be expressed by a function of angular frequency ω as follow

$$f(t) = F_0 + \sum_{h=1}^{\infty} f_h(t) = \frac{1}{2}a_0 + \sum_{h=1}^{\infty}\left\{a_h\cos(h\omega t) + b_h\sin(h\omega t)\right\} \quad (3\text{-}1)$$

where $F_0 = \frac{1}{2}a_0$ is the average value of $f(t)$ .In Eq. (3-1),

$$a_h = \frac{2}{T}\int_0^T f(t)\cos(h\omega t)\,d(\omega t) \quad h = 0,...,\infty \tag{3-2}$$

$$b_h = \frac{2}{T}\int_0^T f(t)\sin(h\omega t)\,d(\omega t) \quad h = 1,...,\infty \tag{3-3}$$

and

$$\frac{1}{2}a_0 = \frac{1}{T}\int_0^T f(t)\,d(\omega t) \tag{3-4}$$

In Eq. (3-1), h is the harmonic order, and $\omega = \frac{2\pi}{T}$ is the angular frequency of the fundamental of the periodical waveform. Also in Eq. (3-1), each harmonic component [$f_h(t) = a_h\cos(h\omega t) + b_h\sin(h\omega t)$] can be represented as a phasor form in terms of its rms value [1],

$$\mathbf{F}_h = F_h e^{j\gamma_h} \tag{3-5}$$

where the rms magnitude F_h is given by

$$F_h = \sqrt{a_h^{\,2} + b_h^{\,2}} \tag{3-6}$$

and phase γ_h is given by

$$\tan(\gamma_h) = \frac{(-b_h)}{a_h} \tag{3-7}$$

Moreover, by using waveform symmetry, it is possible to simplify the calculations of a_h and b_h. When the periodical function $f(t)$ satisfies Eq. (3-8) or Eq. (3-9), it has odd symmetry or even symmetry respectively.

$$f(-t) = -f(t) \tag{3-8}$$

$$f(-t) = f(t) \tag{3-9}$$

For an odd symmetry function, all $a_h = 0$, while for an even

symmetry function, all $b_h = 0$. When a periodical function satisfies Eq. (3-10), it has half-wave symmetry. A half-wave symmetrical function, only contains components with odd orders, i.e. $a_h = 0$ and $b_h = 0$ for even h. Certain waveforms may be odd or even depending on the time reference position selected.

When a periodical function satisfies both Eq. (3-8) and Eq. (3-10) or both Eq. (3-9) and Eq. (3-10), it is called odd half-wave symmetry or even half-wave symmetry, or in general quarter-wave symmetry.

$$f(t) = -f\left(t + \frac{1}{2}T\right) \tag{3-10}$$

The benefit of use of symmetry is that the calculation of the Fourier series coefficients can be simplified. For instance, the coefficients of consine terms a_h are always zero at any orders of harmonics under the constraint of odd half-wave symmetry, and the coefficients of sine terms exist only at odd harmonics. The summarization of symmetry in Fourier analysis is shown in Table 3-1.

Table 3-1 Summarization of symmetry in Fourier analysis [1].

Symmetry	*Condition Required*	a_h *and* b_h
Even	$f(-t) = f(t)$	$b_h = 0 \quad a_h = \frac{2}{\pi}\int_0^{\pi} f(t)\cos(h\omega t)d(\omega t)$
Odd	$f(-t) = -f(t)$	$a_h = 0 \quad b_h = \frac{2}{\pi}\int_0^{\pi} f(t)\sin(h\omega t)d(\omega t)$
Half-wave	$f(t) = -f\left(t+\frac{1}{2}T\right)$	$a_h = b_h = 0$ for even h $a_h = \frac{2}{\pi}\int_0^{\pi} f(t)\cos(h\omega t)d(\omega t)$ for odd h $b_h = \frac{2}{\pi}\int_0^{\pi} f(t)\sin(h\omega t)d(\omega t)$ for odd h
Even quarter-wave	Even and half-wave	$b_h = 0$ for all h $a_h = \begin{cases} \frac{4}{\pi}\int_0^{\pi/2} f(t)\cos(h\omega t)d(\omega t) & \text{for odd } h \\ 0 & \text{for even } h \end{cases}$
Odd quarter-wave	Odd and half-wave	$a_h = 0$ for all h $b_h = \begin{cases} \frac{4}{\pi}\int_0^{\pi/2} f(t)\sin(h\omega t)d(\omega t) & \text{for odd } h \\ 0 & \text{for even } h \end{cases}$

3.2.1 The theory of selective harmonic elimination with quarter-wave symmetric constraint

For illustrating the concept of SHE, we use the most familiar formulation which constructs an output waveform by notching a pre-existing square wave with each notch representing a harmonic controlled. Fig. 3-1 shows a two-level, odd-quarter-wave symmetry waveform with i independent notch angles, $\alpha_1, \alpha_2, \ldots, \alpha_i$. The first step of SHE strategy is to derive a nonlinear transcendental equation set corresponding to the harmonic components which we are interested in.

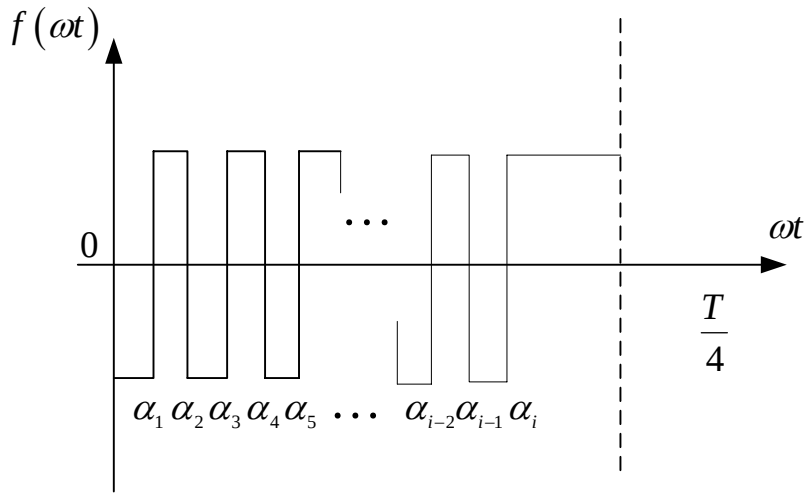

Fig. 3-1 A two-level quarter-wave symmetry waveform.

Conducting Fourier series analysis on the waveform shown in Fig. 3-1, a transcendental equation set involving i equations is given in the following

$$\begin{bmatrix} f_{h_1}(\alpha_1,\alpha_2\cdots,\alpha_i) \\ f_{h_2}(\alpha_1,\alpha_2\cdots,\alpha_i) \\ \vdots \\ f_{h_p}(\alpha_1,\alpha_2\cdots,\alpha_i) \end{bmatrix} = \begin{bmatrix} m_{h_1} \\ m_{h_2} \\ \vdots \\ m_{h_p} \end{bmatrix} \tag{3-11}$$

In Eq. (3-11), f_{h_p} is the p-th equation describing magnitude of the h-th harmonic component m_{h_p}. Corresponding to i notch angles, there are i harmonic components can be controlled. Generally, fundamental component is specified to be a certain value while other $i-1$ harmonics are set to zero. Moreover, by solving the equation set of Eq. (3-11) through some numerical solvers, it is able to obtain the switching angles needed. The desired fundamental magnitude and $i-1$ harmonic eliminations are then achieved by turning on and off the switches in the inverter at adequate time which is relative to the i notch angles.

3.2.2 The theory of selective harmonic elimination with half-wave symmetric constraint

However, the quarter-wave symmetry assumption is not absolutely necessary. A more general formulation can be adapted by changing the quarter-wave symmetry constraint to half-wave symmetry. For illustrating the difference between quarter-wave symmetry and half-wave symmetry, we first consider a two-level quarter-wave symmetry waveform with three notch angles as shown in Fig. 3-2(a). This waveform can be decomposed into four separated waveforms, including one fixed square wave and three quasi-square waves, each one corresponding to a notch angle, as shown in Fig. 3-2(b).

Dividing the original waveform by this way is convenient to conduct Fourier series analysis and to explain the concept of phase shift. First, we focus on the first quasi-square wave with notch angle α_1, and it's shown in Fig. 3-3(a). By applying the equations from Table 3-1, the Fourier series of this quasi-square wave is given by

$$f(t)=\sum_{h=1}^{\infty}\frac{4}{h\pi}\times 2\cos(h\alpha_1)\sin(h\omega t) \qquad h=1,3,...\infty \qquad (3\text{-}12)$$

The phasor form for each frequency component can be expressed as

$$\mathbf{F}_h=-j\frac{4}{h\pi}\times 2\cos(h\alpha_1) \qquad h=1,3,...\infty \qquad (3\text{-}13)$$

Being a quarter-wave symmetry waveform, it only contains odd sine terms in its Fourier series. Next, we shift the quasi-square wave in Fig. 3-3(a) by ϕ_1 degrees as shown in Fig. 3-3(b). It is obviously that the shifted quasi-square wave has half-wave symmetry but not quarter-wave symmetry now.

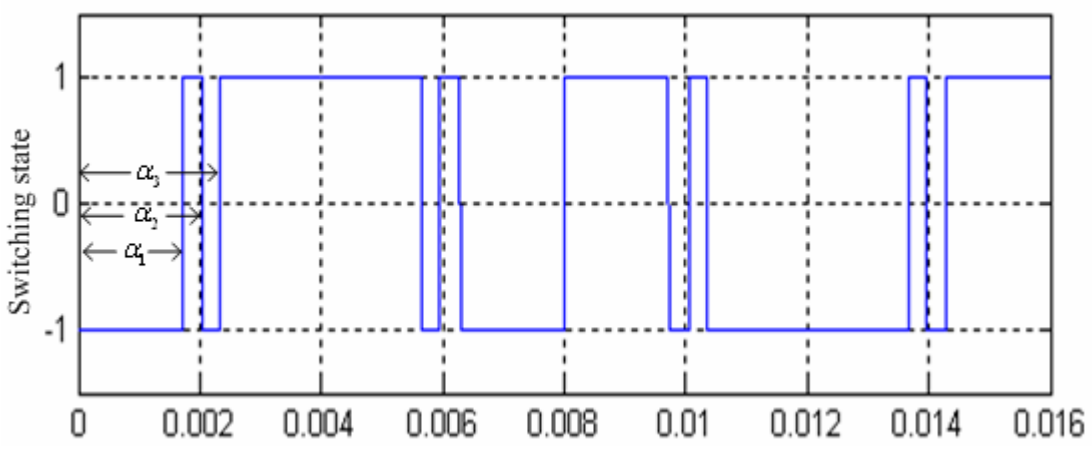

(a)

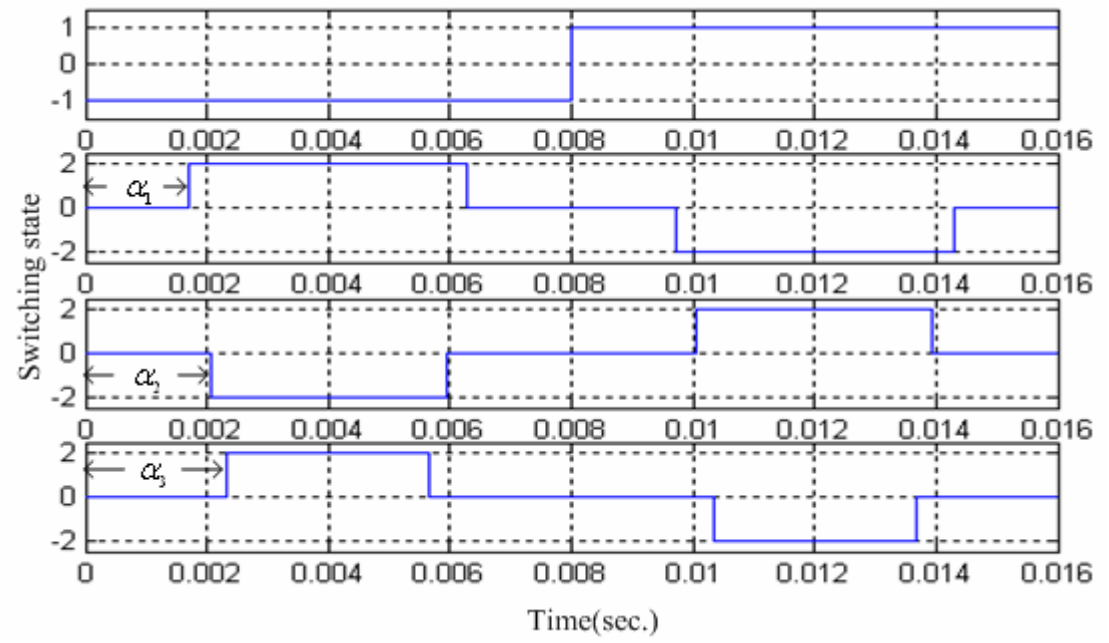

(b)

Fig. 3-2 (a) A two-level quarter-wave symmetry waveform with three notch angles, (b) square wave and quasi-square waves decomposed from (a).

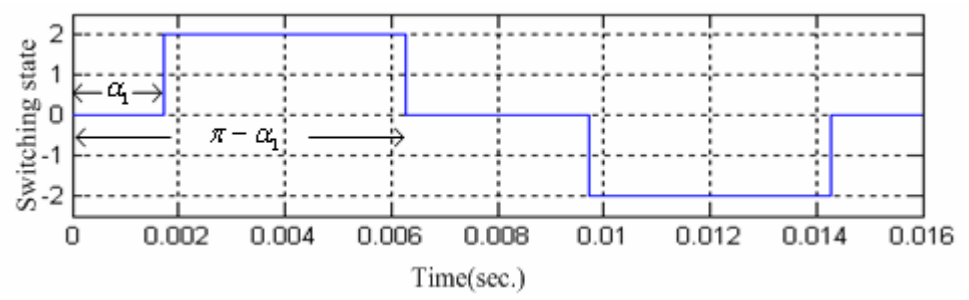

(a)

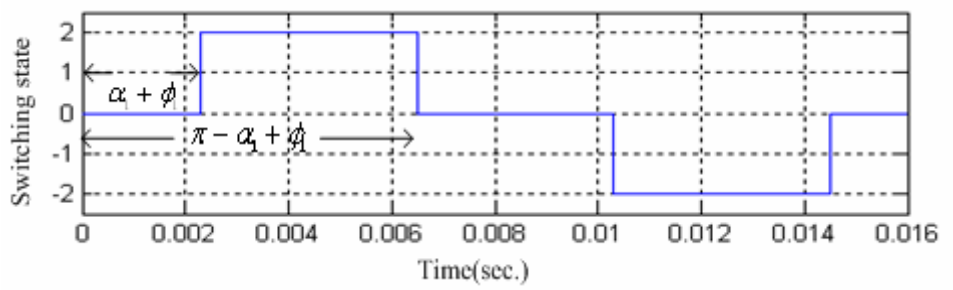

(b)

Fig. 3-3 (a) The quasi-square wave with notch angle α_1. (b) Shifting the quasi-square wave by ϕ_1 degrees.

Again, applying Fourier series analysis on this half-wave symmetric waveform in Fig. 3-3(b), the Fourier series in phasor form can be expressed as

$$F_h^{real} = a_h = -\frac{4}{h\pi} \times 2\cos h\alpha_1 \times \sin h\phi_1 \qquad h = 1,3,...\infty \tag{3-14}$$

$$F_h^{imag} = -b_h = \frac{4}{h\pi} \times 2\cos h\alpha_1 \times \cos h\phi_1 \qquad h = 1,3,...\infty \tag{3-15}$$

$$\mathbf{F_h} = F_h^{real} + jF_h^{imag} \tag{3-16}$$

As odd-symmetry characteristic is no longer existing, the real part, which is corresponding to the even function components, a_h appear. When $\phi_1 = 0$, $F_h^{real} = 0$ and Eq. (3-16) returns to Eq. (3-13). Moreover, we conduct the Fourier series analysis on the rest quasi-square waves with

their corresponding phase-shift angles. The general form for a two-level k-notch half-wave symmetric waveform is given as

$$\mathbf{F}_{h_p}^{\ real} = a_{h_p} = \frac{4}{h_p \pi}(2\sum_{i}^{k}(-1)^i \cos h_p \alpha_i \times \sin h_p \phi_i) \qquad h = 1,3,...\infty \tag{3-17}$$

$$\mathbf{F}_{h_p}^{\ imag} = -b_{h_p} = -\frac{4}{h_p \pi}(1 + 2\sum_{i}^{k}(-1)^i \cos h_p \alpha_i \times \cos h_p \phi_i) \qquad h = 1,3,...\infty \tag{3-18}$$

where h_p is the p-th element in a set of controlled harmonics h having k elements, α is a vector of length k with each element α_i representing the ith notching, ϕ is a vector of length k with each element ϕ_i representing the phase-shift angle corresponding to the i-th quasi-square wave. The harmonic content can also be described in polar coordinate such that

$$F_h^{\ real} = m_p \cos(\gamma_p) \tag{3-19}$$

$$F_h^{\ imag} = m_p \sin(\gamma_p) \tag{3-20}$$

where m_p is the magnitude and γ_p is the phase of the p-th harmonic. It should be noted that Eq. (3-17) and Eq. (3-18) are constructed by a fixed square wave and k quasi-square waves. Even the harmonic phase γ_p varies, the square wave is still fixed. Only the α_i and ϕ_i are variables. If there are k notch angles in the period of first quarter, it will generate $2k$ variables including k notch angles and k phase-shift angles. It brings k controllable conditions. These k controllable

conditions result in $2k$ equations, k real part equations and k image part equations respectively. Being a nonlinear equation set, it can be solved by some numerical solvers such as Newton-Rephson method which provides faster convergence speed. In this thesis, a waveform with 3 notch angles and 3 corresponding phase-shift angles are considered, and the desired fundamental amplitude, zero 11_{th} harmonic and zero 13_{th} harmonic are the three conditions.

The equation set for this problem considered in this thesis is given by

$$F(\alpha,\phi)=\begin{bmatrix} \frac{4}{\pi}(-2\cos\alpha_1\times\sin\phi_1+2\cos\alpha_2\times\sin\phi_2-2\cos\alpha_2\times\sin\phi_2) \\ \frac{4}{11\pi}(-2\cos 11\alpha_1\times\sin 11\phi_1+2\cos 11\alpha_2\times\sin 11\phi_2-2\cos 11\alpha_2\times\sin 11\phi_2) \\ \frac{4}{13\pi}(-2\cos 13\alpha_1\times\sin 13\phi_1+2\cos 13\alpha_2\times\sin 13\phi_2-2\cos 13\alpha_2\times\sin 13\phi_2) \\ \frac{4}{\pi}(-1+2\cos\alpha_1\cos\phi_1-2\cos\alpha_2\cos\phi_2+2\cos\alpha_3\cos\phi_3) \\ \frac{4}{11\pi}(-1+2\cos 11\alpha_1\cos 11\phi_1-2\cos 11\alpha_2\cos 11\phi_2+2\cos 11\alpha_3\cos 11\phi_3) \\ \frac{4}{13\pi}(-1+2\cos 13\alpha_1\cos 13\phi_1-2\cos 13\alpha_2\cos 13\phi_2+2\cos 13\alpha_3\cos 13\phi_3) \end{bmatrix}$$

$$=\begin{bmatrix} m_1\cos(\gamma_1) \\ m_{11}\cos(\gamma_{11}) \\ m_{13}\cos(\gamma_{13}) \\ m_1\sin(\gamma_1) \\ m_{11}\sin(\gamma_{11}) \\ m_{13}\sin(\gamma_{13}) \end{bmatrix} \qquad (3\text{-}21)$$

Then, Eq. (3-21) can be modified as

$$\begin{bmatrix} -2\cos\alpha_1 \times \sin\phi_1 + 2\cos\alpha_2 \times \sin\phi_2 - 2\cos\alpha_2 \times \sin\phi_2 \\ -2\cos 11\alpha_1 \times \sin 11\phi_1 + 2\cos 11\alpha_2 \times \sin 11\phi_2 - 2\cos 11\alpha_2 \times \sin 11\phi_2 \\ -2\cos 13\alpha_1 \times \sin 13\phi_1 + 2\cos 13\alpha_2 \times \sin 13\phi_2 - 2\cos 13\alpha_2 \times \sin 13\phi_2 \\ -1 + 2\cos\alpha_1 \cos\phi_1 - 2\cos\alpha_2 \cos\phi_2 + 2\cos\alpha_3 \cos\phi_3 \\ -1 + 2\cos 11\alpha_1 \cos 11\phi_1 - 2\cos 11\alpha_2 \cos 11\phi_2 + 2\cos 11\alpha_3 \cos 11\phi_3 \\ -1 + 2\cos 13\alpha_1 \cos 13\phi_1 - 2\cos 13\alpha_2 \cos 13\phi_2 + 2\cos 13\alpha_3 \cos 13\phi_3 \end{bmatrix}$$

$$= \frac{\pi}{4} \begin{bmatrix} m_1 \cos(\gamma_1) \\ 11 \times m_{11} \cos(\gamma_{11}) \\ 13 \times m_{13} \cos(\gamma_{13}) \\ m_1 \sin(\gamma_1) \\ 11 \times m_{11} \sin(\gamma_{11}) \\ 13 \times m_{13} \sin(\gamma_{13}) \end{bmatrix} \tag{3-22}$$

To satisfy these three conditions described above, m_1 is substituted by the desired fundamental magnitude, which is relative to the amplitude modulation index m_1, and both m_{11} and m_{13} are set to zero. The last controllable factor γ_1 is free to vary. In order to get the continuous solution, we conduct the Newton iteration every two degrees of the fundamental phase γ_1 varied from 0 to 360 degrees. The variation of γ_1 does not change the harmonic magnitude of the controlled harmonics, but the uncontrolled harmonics is changed. The next two lowest order harmonics in this system are 23_{th} and 25_{th} harmonics that can be attenuated by adequate phase change. In next section, the method of solving Eq. (3-22) will be illustrated.

3.3 Numerical solver

Because the equation set derived from Fourier series analysis is transcendental, solving the accurate answer is not possible. But it is still possible to be solved in reasonable accuracy. Newton-Rephson iteration method is chose for solving this nonlinear equation set in this thesis due to its faster convergence speed.

3.3.1 Newton's method for systems

Suppose that a transformation $\mathbf{T}: \boldsymbol{R}^2 \to \boldsymbol{R}^2$ is given, where

$$\mathbf{T}(x,y) = \left(f(x,y), g(x,y) \right) \tag{3-23}$$

for some continuous functions f and g. Consider $\mathbf{T}(\mathbf{v}^0 + \mathbf{h}) - \mathbf{T}(\mathbf{v}^0)$, where $\mathbf{v^0} = (x^0, y^0)$ is a point in the domain of $\mathbf{T}$ and $\|\mathbf{h} = (h_1, h_2)\|$ is sufficiently small so that point $\mathbf{v}^0 + \mathbf{h}$ is still in the domain of $\mathbf{T}$. Clearly,

$$\begin{aligned} T(\mathbf{v}^0 + \mathbf{h}) - T(\mathbf{v}^0) = \big(& f(x_0 + h_1, y_0 + h_2) \\ & - f(x_0, y_0), g(x_0 + h_1, y_0 + h_2) - g(x_0, y_0) \big) \end{aligned} \tag{3-24}$$

We know from calculus that under the conditions given,

$$f(x_0 + h_1, y_0 + h_2) - f(x_0, y_0) \cong f_x(x_0, y_0) h_1 + f_y(x_0, y_0) h_2 \tag{3-25}$$

and

$$g(x_0 + h_1, y_0 + h_2) - g(x_0, y_0) \cong g_x(x_0, y_0) h_1 + g_y(x_0, y_0) h_2 \tag{3-26}$$

Combining results, we find that

$$T(\mathbf{v}^0 + \mathbf{h}) - T(\mathbf{v}^0) \cong \begin{bmatrix} f_x(x_0, y_0) & f_y(x_0, y_0) \\ g_x(x_0, y_0) & g_y(x_0, y_0) \end{bmatrix} \begin{bmatrix} h_1 \\ h_2 \end{bmatrix} \tag{3-27}$$

We define the matrix

$$\mathbf{J}=\begin{bmatrix} f_x(x_0,y_0) & f_y(x_0,y_0) \\ g_x(x_0,y_0) & g_y(x_0,y_0) \end{bmatrix} \tag{3-28}$$

to be the derivative of transformation **T** at point $\mathbf{v}^0$. It's called Jocobian matrix in most literatures. In summary, we have

$$\mathbf{T}(\mathbf{v}^0+h)-\mathbf{T}(\mathbf{v}^0)\cong \mathbf{Jh} \tag{3-29}$$

Now consider the nonlinear system $\mathbf{T}(\mathbf{v})$ =0. Suppose that $\mathbf{v^0}=(x^0,y^0)$ is an approximation of solution **R**. Now

$$\mathbf{T}(\mathbf{R})-\mathbf{T}(\mathbf{v}^0)\cong \mathbf{J}(\mathbf{R}\text{-}\mathbf{v}^0) \tag{3-30}$$

so

$$-\mathbf{T}(\mathbf{v}^0)\cong \mathbf{J}(\mathbf{R}\text{-}\mathbf{v}^0) \tag{3-31}$$

If $(\mathbf{JT})^{-1}$ exists, then we find

$$-\mathbf{J}^{-1}\mathbf{T}(\mathbf{v}^0)\cong \mathbf{R}\text{-}\mathbf{v}^0 \tag{3-32}$$

and

$$\mathbf{R}\cong \mathbf{v}^0\text{-}\mathbf{J}^{-1}\mathbf{T}(\mathbf{v}^0) \tag{3-33}$$

We expect that the vector $\mathbf{v}^0\text{-}\mathbf{J}^{-1}\mathbf{T}(\mathbf{v}^0)$ will be a better approximation to the root **R** than the initial estimate $\mathbf{v}^0$. According to the illustration above, the iteration equation can be described as

$$\mathbf{v}^{n+1}=\mathbf{v}^n-\left(\mathbf{J}(\mathbf{v}^n)\right)^{-1}\mathbf{T}(\mathbf{v}^n) \tag{3-34}$$

where the vector **v** contains all variables, α_i and ϕ_i.

3.3.2 Implementation of Newton's method by Matlab

In this thesis, the calculation work is implemented by the mathematical software Matlab. Program editing is based on the following

steps.

Step1 Setting the initial vector

The first step of implementing iteration is setting the initial vector. Then, the adequate approximation root will be found after a few iterations. However, if the position of initial point is not good, it will result in divergence. The iteration starts with many different initial vectors in order to find possible root anywhere.

Step2 Iteration

After setting the initial vector, the next step is performing the iteration. There are two conditions to stop the iteration. If the number of iterations is larger than a maximum default value in the program, the iteration will stop. Or, when the tolerated error $\Delta\mathbf{v}$, described by Eq. (3-35), is small than the tolerated default value in the program, the iteration will stop as well.

$$\Delta\mathbf{v} = \mathbf{v}^{n+1} - \mathbf{v}^{n} \tag{3-35}$$

Step3 Selecting the result solutions

The different initial value results in different solutions. The solutions we want have to meet the conditions below, otherwise they will be ignored.

$$0 \le \alpha_1 \le \alpha_2 \cdots \le \alpha_i < 90 \tag{3-36a}$$

$$(\alpha_1 + \phi_1) < (\alpha_2 + \phi_2) \ldots < (\alpha_i + \phi_i) \tag{3-36b}$$

$$(\pi - \alpha_i + \phi_i) < (\pi - \alpha_{i-1} + \phi_{i-1}) \ldots < (\pi - \alpha_1 + \phi_1) \tag{3-36c}$$

One set of the solutions at unit fundamental and the $\gamma_1 = 0$ is shown

in Table 3-2. Because the nonlinear functions are continuous, we can obtain the solutions at $\gamma_1 = 2^\circ$ and unit fundamental by setting the initial values derived from previous result at $\gamma_1 = 0^\circ$.

Table 3-2 The solutions at unit fundamental and $\gamma_1 = 0$.

α_1	α_2	α_3	ϕ_1	ϕ_2	ϕ_3
17.226	19.718	28.487	0	0	0

Similarly, γ_1 is incremented step by step and the solutions obtained from the present step are used as initial values for the next step. In this thesis, to perform the continuity of the result solution and to avoid divergence, the incremental scale is 2 degrees. The solutions, three notch angles and three corresponding phase-shift angles, for γ_1 varying from 0° to 360° with fundamental remaining unity are show in Fig. 3-4 and Fig. 3-5.

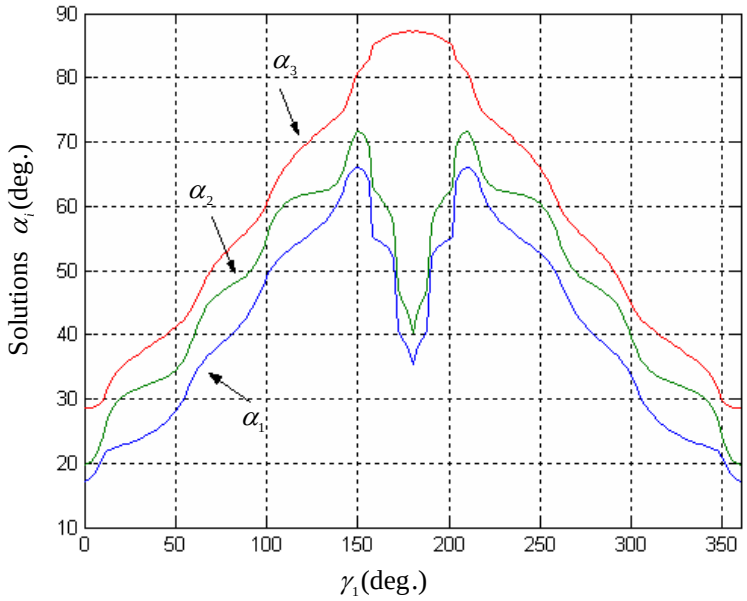

Fig. 3-4 Solutions α_i at a modulation index of 1.0 as γ_1 varying from 0° to 360° with harmonic control of eliminating 11-th and 13-th harmonics.

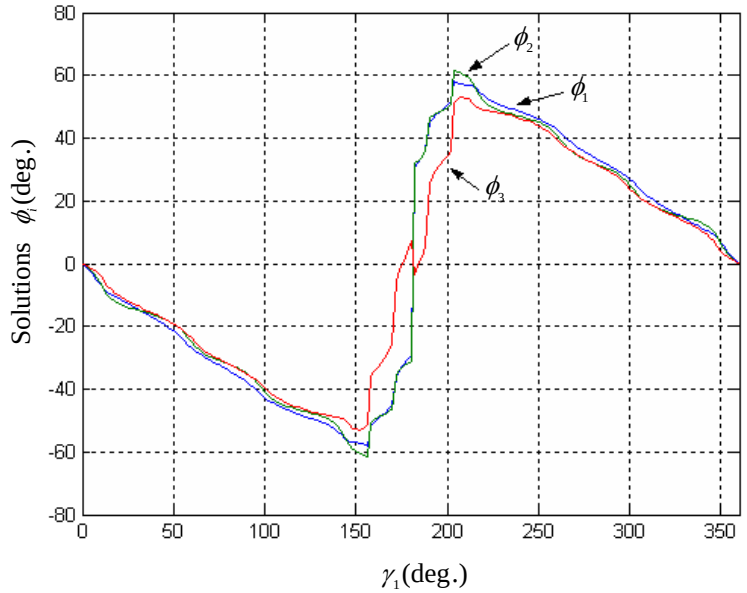

Fig. 3-5 Three corresponding phase-shift angles of each quasi-square wave at unit modulation index as γ_1 varying from 0° to 360° with harmonic control of eliminating 11-th and 13-th harmonics.

It's worthy to mention that the solutions of α_i are symmetric to the vertical line through 180 degrees and the solutions of ϕ_i are symmetric to the point of $\gamma_1 = 180^\circ$ and $\phi = 0^\circ$. These relationships simplify the calculation work and only the first half range of γ_1 needs to deal with. These symmetric relationships are described in Eq. (3-37) and Eq. (3-38).

$$\alpha_i(\pi + \psi) = \alpha_i(\pi - \psi) \tag{3-37}$$

$$\phi_i(\pi + \psi) = -\phi_i(\pi - \psi) \tag{3-38}$$

where the ψ can take any value from 0° to 180°.

Next, the same processes are used to solve this problem at different indexes. Whenever the modulation index is incremented or decreased, the problem is solved by using the previous solutions as initial values for the next step. After solving the problem over the whole ranges of m_1 and γ_1, the solutions of three notch angles and three corresponding phase-shift angles can be represented by 6 3-dimension graphs as shown in Fig. 3-6(a) to Fig. 3-6(f). In each 3-dimension graph, x-axis and y-axis are denoted as m_1 and γ_1 respectively, while z-axis is denoted as the solution angle.

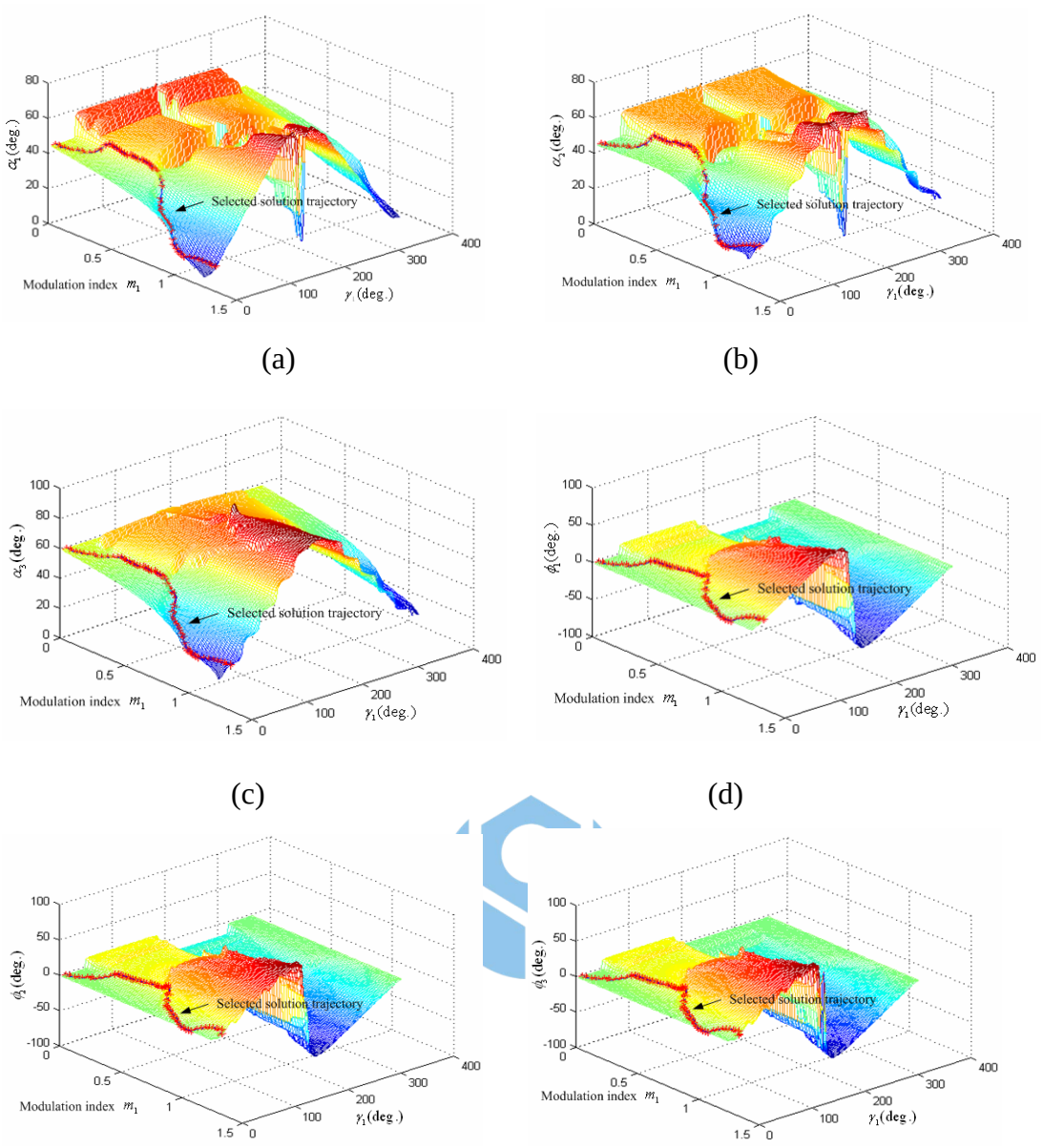

(a) (b)

(c) (d)

(e) (f)

Fig. 3-6 3-dimension graphs of the solution angles. (a) α_1, (b) α_2, (c) α_3, (d) ϕ_1, (e) ϕ_2, (f) ϕ_3.

For checking the effect of the phase shift of the fundamental, now we compare two cases with same conditions except γ_1. Fig.3-7 shows the notched waveform at m_1=0.5 and $\gamma_1 = 0$. Obviously, the 11-th and 13-th harmonics are almost eliminated, and the fundamental is controlled at 0.5.

The 23-rd and 25-th harmonics, being about 70% and 27% of the fundamental respectively, are what we desire to suppress by phase shift. Fig. 3-8 shows the other notched waveform and its spectrum at modulation index of 0.5 and the phase γ_1 of 50 degrees. Comparing with the former case, now the 23-th and 25-th harmonics are down to 28% and 20% with the same fundamental and, 11-th and 13-th harmonics being eliminated. Besides, in both Fig. 3-7 and Fig. 3-8, it is obviously that amplitudes of harmonic orders below 23-th are quite large. However, attributed to the zig-zag transformers, these harmonics will all be trapped in the transformers and not appear in the output line-to-line voltage waveform.

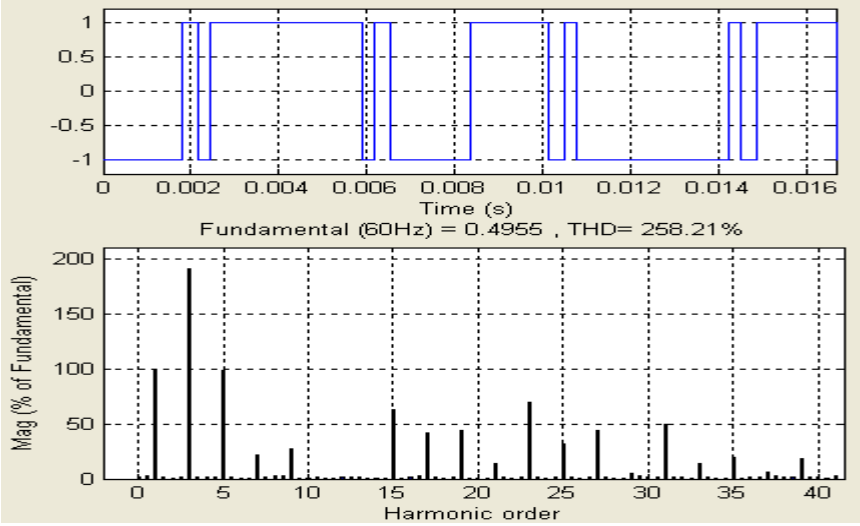

Fig. 3-7 The waveform at a modulation index of 0.5 as $\gamma_1 = 0^\circ$ with harmonic control of eliminating 11-th and 13-th harmonics.

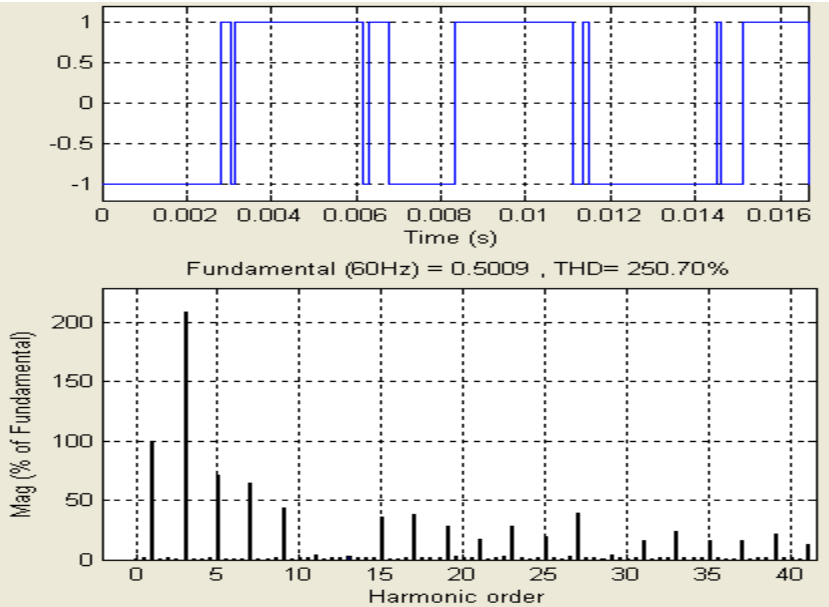

Fig. 3-8 The waveform at a modulation index of 0.5 as $\gamma_1 = 50^\circ$ with harmonic control of eliminating 11-th and 13-th harmonics.

The strategy to choose the most suitable phase shifts of γ_1 for this system at any modulation index is discussed in next section.

3.4 Selection of fundamental phases γ_1

According to the discussion in the previous section, the harmonic distribution changes by varying the fundamental phase γ_1. This gives us the opportunity to choose suitable solutions with respect to γ_1 which minimizes 23-rd and 25-th harmonics. Therefore, the root-sum-square (rss) values of 23-rd and 25-th harmonics, denoted as $V_{23,25}$, contained in the output line-to-line voltage are calculated over the full ranges of m_1 and γ_1. Fig. 3-9(a) shows the contour map of the $V_{23,25}$ and its 3-D diagram also shows in Fig. 3-9(b). Over the whole range of m_1 we can depict many profiles of $V_{23,25}$ with respect to specified m_1. Fig.3-10

shows the profile of the $V_{23,25}$ corresponding to m_1 =0.5 and it is obviously that the minimum $V_{23,25}$ occurs at $\gamma_1 = 50°$ and $\gamma_1 = 310°$. It is already described in last section that the solution of the notch angles are symmetric to $\gamma_1 = 180°$, therefore all profiles are symmetric to $\gamma_1 = 180°$ as well. After searching the contour, the route with the minimum $V_{23,25}$ over the whole range of m_1 is identified as route A in Fig. 3-9(a), which has the lowest height at any modulation index. However, route A is seriously tortuous and is not suitable for on-line calculation by curve-fitting approximation, which will be employed later in this paper. Therefore, finding another routes with both relative-low $V_{23,25}$ and acceptable smoothness are necessary. According to this strategy, a smoother route is chosen and marked as route B in Fig. 3-9(a). Along route B, even its $V_{23,25}$ are not the lowest ones, but it provides moderate smoothness so that on-line calculation based on curve-fitting approximation can be implemented easily. Once the route is decided, the solutions of notch angles corresponding to the chosen route can also compose another six routes which are shown in Fig. 3-6 (a)-(f) by marking signs. By taking the end view into the $\alpha_1 - m_1$ plane, we can re-depict route $B_{\alpha 1}$ in Fig.3-6(a) as functions of m_1 for convenience. Then, taking the same process on the other 5 routes in Fig.3-6, the relationships between six solution angles and m_1 are shown in Fig. 3-11. Although we can establish a set of tables according to Fig.3-11 and store

them in

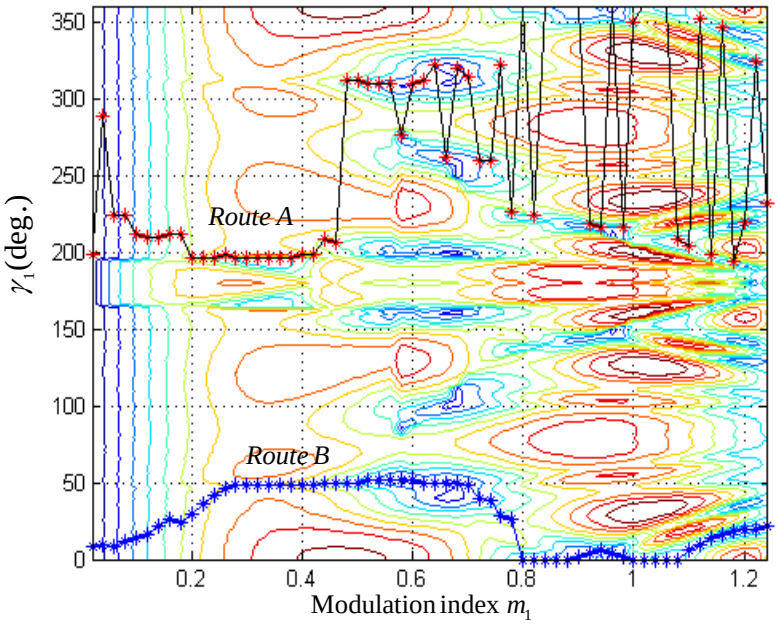

(a)

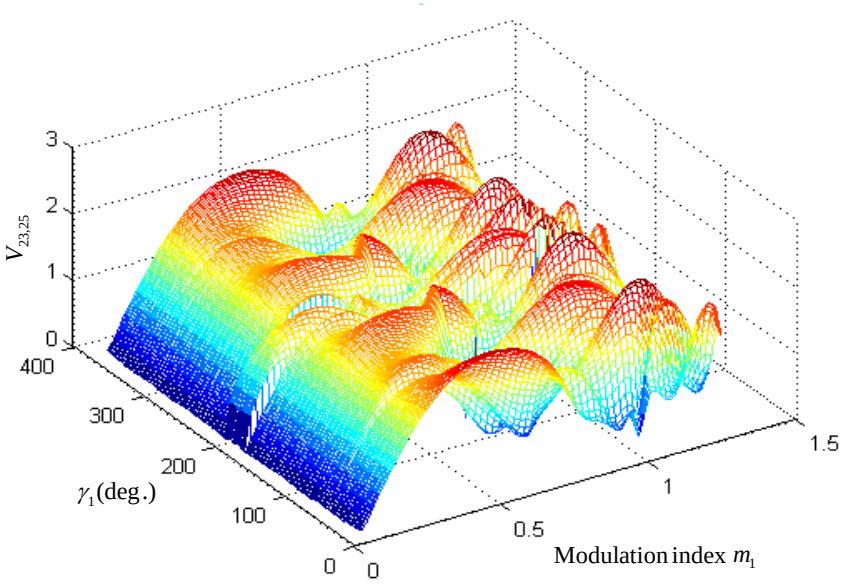

(b)

Fig. 3-9(a) The contour of the rss values of the 23-th and 25-th harmonics, (b) 3-D graph of the rss values of the 23-th and 25-th harmonics.

system's memory, we will apply curve-fitting approximation based on the results in Fig. 3-11 to implement on-line calculation for the proposed system in the next section.

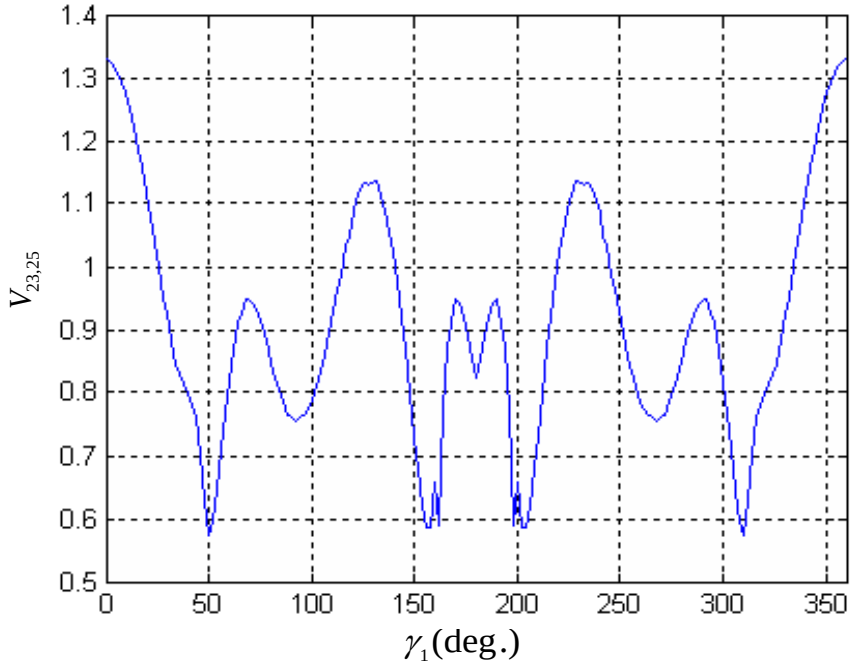

Fig. 3-10 The profile of rss values of the 23-th and 25-th harmonics at m_1=0.5.

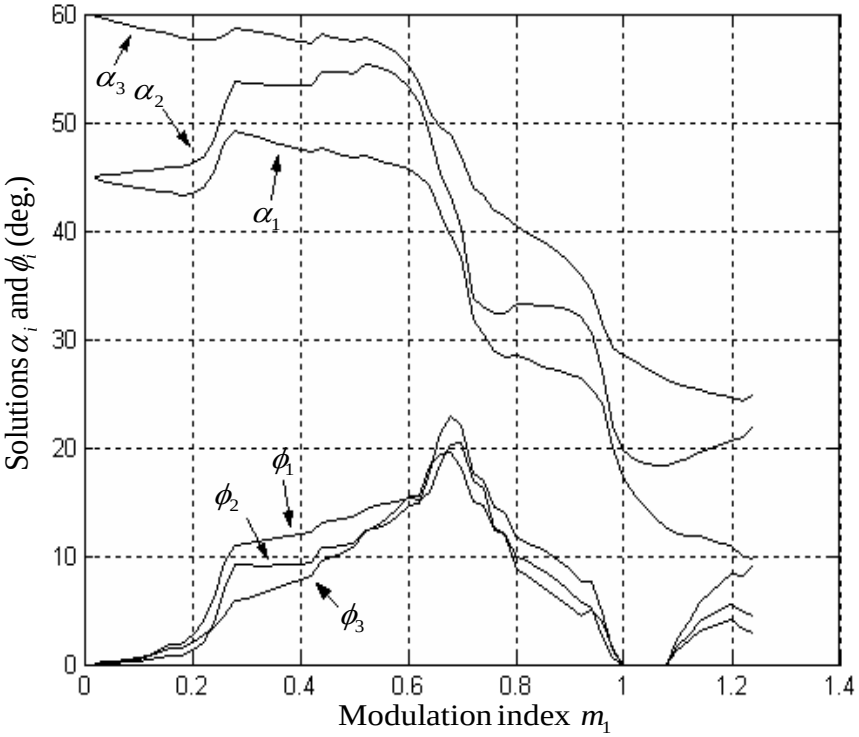

Fig. 3-11 The relationships between six solution angles and m_1 corresponding to route B.

3.5 On-line calculation of the approximated polynomial derived by curve-fitting method

In this section, the approximated-polynomial curve fitting based on least-squares method will be investigated to implement on-line calculation for notch angles. The errors between accurate notch angles and approximated polynomials are dependent on the number of the order of the polynomials. The lower order polynomials the larger error. However, the higher order polynomials the longer process time. Another approach is dividing the exact data into several segments and each segment has individual polynomial with lower order. The comparison between the single high-order polynomial approximation and the piecewise-continuous second-order polynomial approximation is demonstrated in this section.

3.5.1 The least-squares solution

Let (x_1, y_1), (x_2, y_2),…, (x_n, y_n) be a set of paired practical data. Suppose that the u-order $(u \le n)$ polynomial

$$y(x) = a_0 + a_1 x + a_2 x^2 + \cdots + a_u x^u \tag{3-39}$$

is the ‘‘best fit’’ for this set of data. One strategy for best fit is to minimize the sum of the squares of the residuals

$$E = \sum_{i=1}^{n} \left(y_i - a_0 - a_1 x_i - a_2 x_i^{\,2} - \cdots - a_u x_i^{\,u} \right)^2 \tag{3-40}$$

We must have

$$\frac{\partial E}{\partial a_i} = 0, \qquad i = 1, \ldots, u$$

And for each coefficient,

$$\frac{\partial E}{\partial a_0} = -2\sum_{i=1}^{n}\left(y_i - a_0 - a_1 x_i - a_2 x_i^{\,2} - \cdots - a_u x_i^{\,u}\right)$$

$$\frac{\partial E}{\partial a_1} = -2\sum_{i=1}^{n} x_i\left(y_i - a_0 - a_1 x_i - a_2 x_i^{\,2} - \cdots - a_u x_i^{\,u}\right) \qquad (3\text{-}41)$$

$$\vdots$$

$$\frac{\partial E}{\partial a_m} = -2\sum_{i=1}^{n} x_i^{\,u}\left(y_i - a_0 - a_1 x_i - a_2 x_i^{\,2} - \cdots - a_u x_i^{\,u}\right)$$

by setting these equations to zero, we have

$$\begin{aligned} a_0 n + a_1\sum x_i + a_2\sum x_i^{\,2} + \cdots + a_m\sum x_i^{\,u} &= \sum y_i \\ a_0\sum x_i + a_1\sum x_i^{\,2} + \cdots + a_m\sum x_i^{\,u+1} &= \sum x_i y_i \qquad (3\text{-}42) \\ &\vdots \\ a_0\sum x_i^{\,u} + a_1\sum x_i^{\,u+1} + \cdots + a_u\sum x_i^{\,2u} &= \sum x_i^{\,u} y_i \end{aligned}$$

(where $\sum$ denotes the summation from $i=1$ to n).

Setting $\sum x_i^{\,k} = s_k, k = 0,1,\ldots,2u$, and denoting the entries of the right-hand side, respectively, by $b_0, b_1, \ldots, b_u$, the equations can be written as

$$\begin{bmatrix} s_0 & \cdots & s_u \\ s_1 & \cdots & s_{u+1} \\ \vdots & & \\ s_u & \cdots & s_{2u} \end{bmatrix} \begin{bmatrix} a_0 \\ a_1 \\ \vdots \\ a_u \end{bmatrix} = \begin{bmatrix} b_0 \\ b_1 \\ \vdots \\ b_u \end{bmatrix} \qquad (3\text{-}43)$$

(Note that $s_0 = n$.) Define

$$\mathbf{V} = \begin{bmatrix} 1 & x_1 \cdots & x_1^{\,u} \\ 1 & x_2 \cdots & x_2^{\,u} \\ \vdots & \vdots & \vdots \\ 1 & x_n \cdots & x_n^{\,u} \end{bmatrix} \tag{3-44}$$

Then this system is equal to

$$\mathbf{V}^T\mathbf{V}\mathbf{a} = \mathbf{b} = \mathbf{V}^T\mathbf{y}$$

where $\mathbf{a} = \begin{bmatrix} a_0 \\ \vdots \\ a_u \end{bmatrix}$ $\mathbf{b} = \begin{bmatrix} b_0 \\ \vdots \\ b_u \end{bmatrix}$ $\mathbf{y} = \begin{bmatrix} y_1 \\ \vdots \\ y_n \end{bmatrix}$ (3-45)

then the polynomial coefficients can be solved by

$$\mathbf{a} = \left(\mathbf{V}^T\mathbf{V}\right)^{-1}\mathbf{V}^T\mathbf{y} \tag{3-46}$$

The $n \times u$ matrix **V** stores the modulation index of fundamental, and the matrix **y** stores the data of solutions (α_i and/or ϕ_i) at each modulation depth. For each solution (α_i and/or ϕ_i), there are n data points solved by precise calculation described in previous section. The trajectory formed by the n data points is represented by a u-order polynomial obtained by the curve-fitting approach with an equation in terms of m_1. MATLAB's curve fitting function based on polynomial regression is suitable as a tool to approximate these trajectories. Therefore, each trajectory is modeled by a polynomial equation in the form of

$$\alpha_h(m_1) = a_0 + a_1 m_1 + a_2 m_1^{\,2} + \ldots + a_u m_1^{\,u} \tag{3-47}$$

where u is the polynomial order. The unknown coefficients ($a_0, a_1, a_2 \ldots, a_u$) are computed by doing a least square fit which minimizes the sum of squares of the deviations between the practical data and the

data derived from the approximated *u*-order polynomial.

3.5.2 Error Analysis of high-level polynomial approximation

In this thesis, a more meaningful error expression, caused by trajectory deviation between accurate data and approximated data derived from curve-fitting method, is described by

$$\varepsilon_h = \frac{m_h - m_h'}{m_1} \times 100\% \tag{3-48}$$

where ε_h is the error of the *h*-th harmonic magnitude expressed as a percentage of the fundamental solved by precise solution, m_h is the magnitude of *h*-th harmonic derived from substituting the variables of Eq. 3-22 by the precise solutions solved by the nonlinear transcendental equations, and m_h' is the magnitude of the *h*-th harmonic calculated by substituting the variables of Eq. 3-22 by the solution derived from approximated polynomials.

Since the solution curves illustrated in Fig. 3-11 are rather tortuous, the orders of the approximated polynomials have to be high enough to prevent unacceptable errors. Fig. 3-12 shows the relationship between 6-order polynomial curves, denoted by black line, and the precise solutions, denoted by dotted line. The fundamental 11-th and 13-th harmonic errors caused by trajectory deviation between exact solutions and the solutions derived by 6-order approximated polynomials are shown in Fig. 3-13. Moreover, Fig. 3-14 and Fig. 3-15 show the solution curves and the error diagram with 10-order approximation for comparison. Obviously, the harmonic errors are smaller than the errors derived from 6-order polynomial. Therefore, it’s clear that higher orders of polynomial

causes lower error between experimental data and the data derived from approximated polynomial.

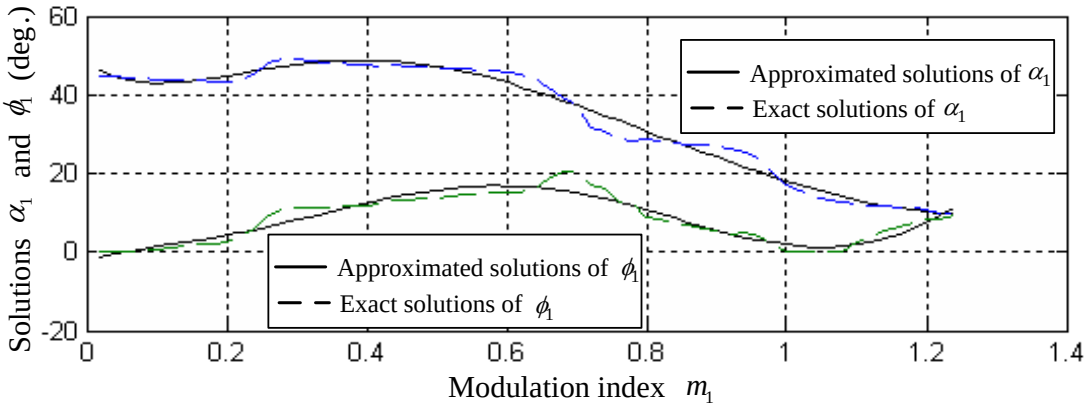

(a)

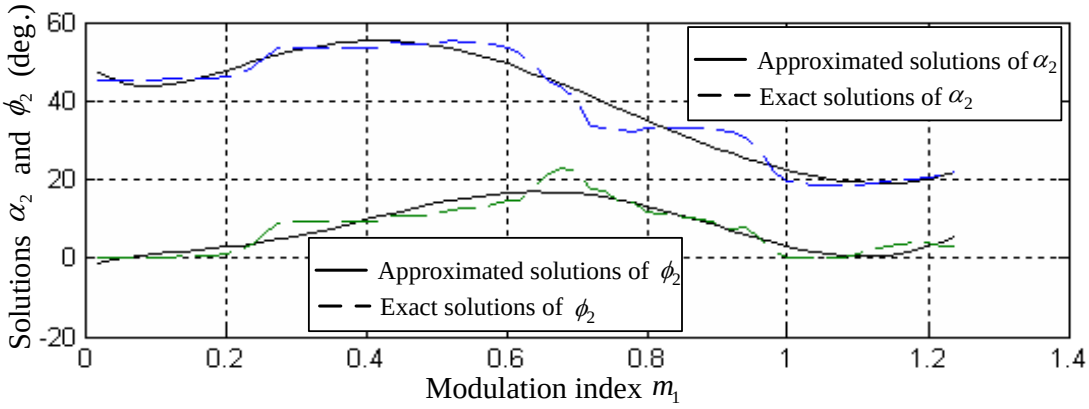

(b)

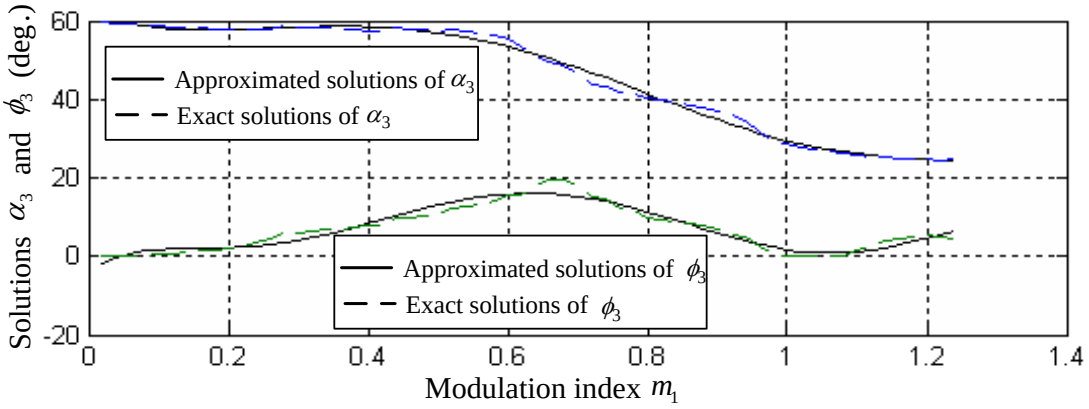

(c)

Fig. 3-12 Relations between 6-order curve-fitting solutions and the exact solutions for α_i and ϕ_i, where $i = 1$(a), 2(b), 3(c).

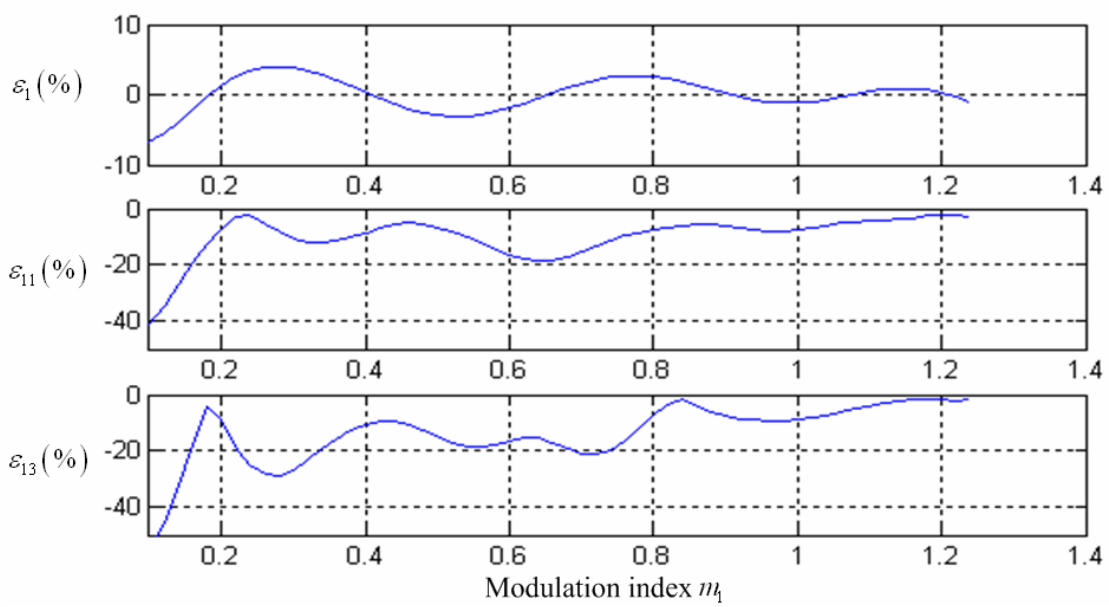

Fig. 3-13 The harmonic error ε_h derived from solutions between exact solutions and the approximated 6-order polynomials.

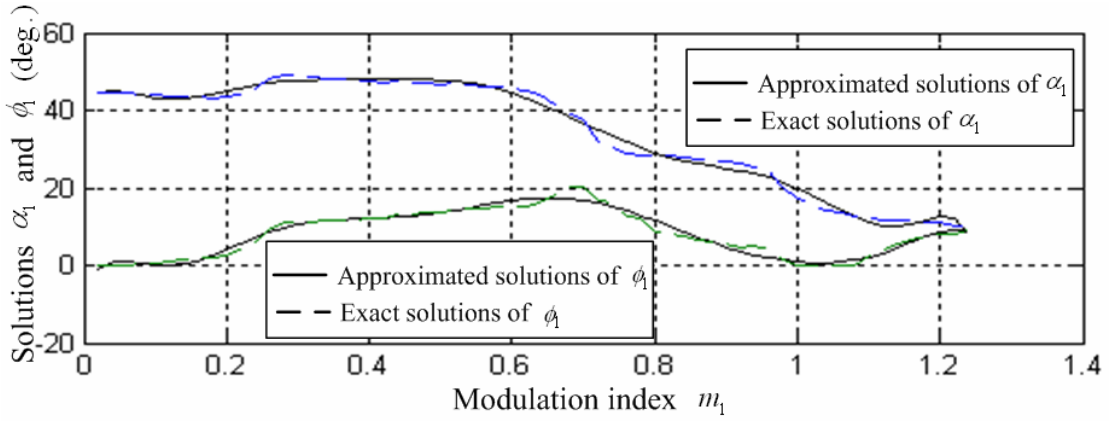

(a)

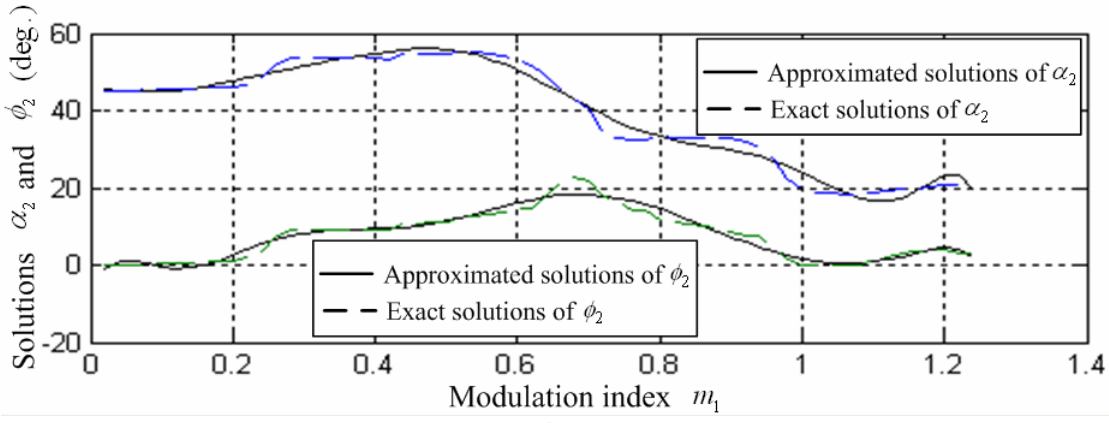

(b)

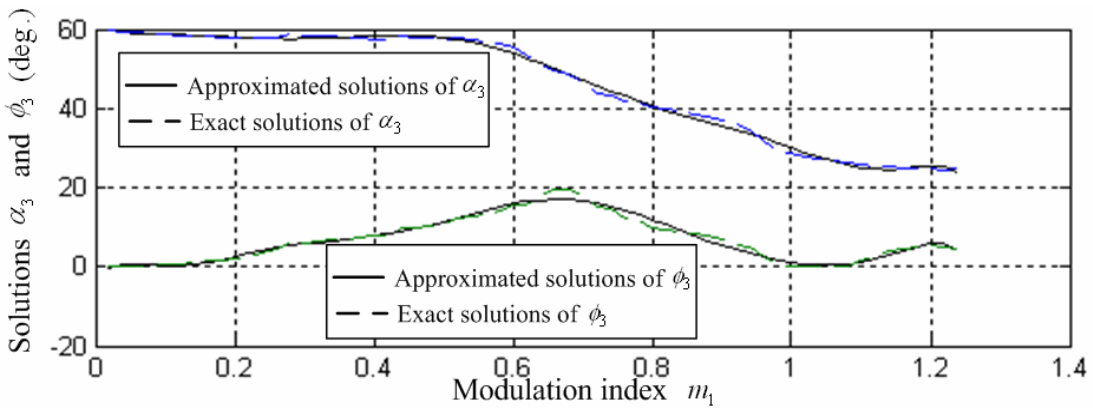

(c)

Fig. 3-14 Relations between 10-order curve-fitting solutions and the exact solutions for α_i and ϕ_i, where $i = 1$(a), 2(b), 3(c).

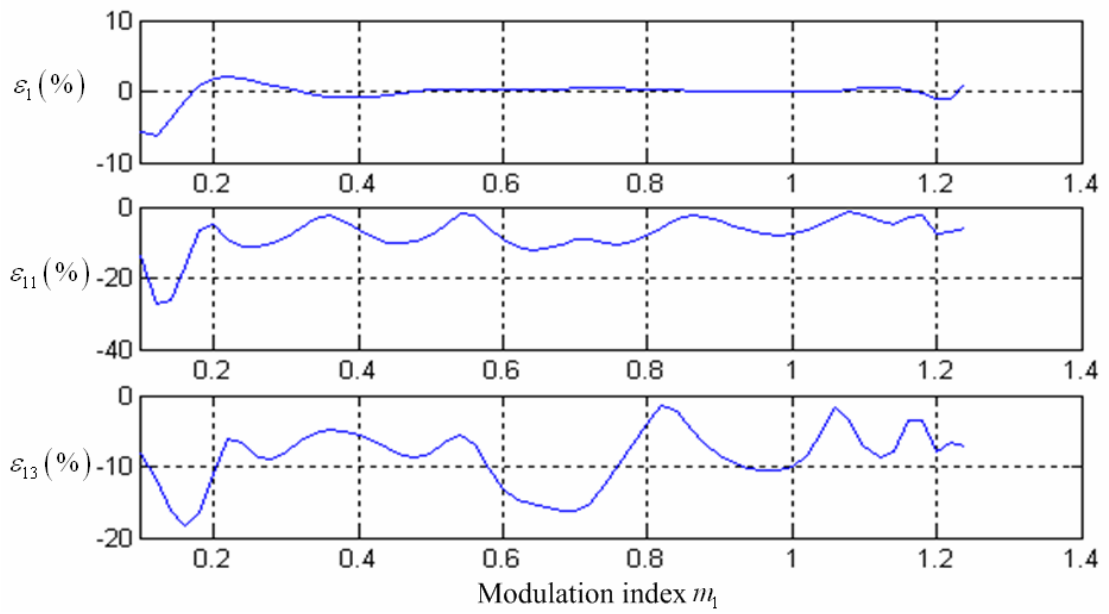

Fig. 3-15 The harmonic error ε_h derived from solutions between exact solutions and the approximated 10-order polynomials.

Form Fig. 3-13 and Fig. 3-15, it can be seen that the errors are rather larger in the range of m_1 less than 0.2, because of the smaller denominator in Eq. 3-48. Therefore, the approximated polynomials are not recommended for use in this range, and can only be applied on some systems where harmonic quality demand isn't so strict. However, for most practical applications modulation depth varying from 0.2 to 1.24 is

quite enough. The summarization of the biggest harmonic errors derived by curve-fitting method from orders of 6 to 10 is shown in Table 3-3 with m_1 from 0.2 to 1.24. Another meaningful parameter called average harmonic error, the average of the harmonic error at every modulation depth, is defined as

$$\varepsilon_{h(avg)} = \frac{1}{N - initial} \sum_{i=initial}^{N} \varepsilon_h^{0.02i} \tag{3-49}$$

where the parameter $\varepsilon_h^{0.02i}$ is the hth harmonic error defined by Eq. (3-45) at the modulation index of $0.02 \times i$, and i starts from the initial data number, $initial$, to the maximum data number *N*. The available error data start from the modulation index of 0.2 to 1.24, so i starts from $initial = 10$ to the maximum data number N =62. The average harmonic errors are summarized in Table 3-4 with polynomial orders from 6 to 10.

Table 3-3 The summarization of the biggest harmonic error derived by curve-fitting method from 6 orders to 10 orders' polynomial.

Orders u	*The maximum harmonic error* $\lvert\varepsilon_h\rvert$ *in % at* m_1 *varied from 0.2 to 1.24*			*The modulation index* m_1 *where the largest error* $\lvert\varepsilon_h\rvert$ *occur*		
	$\lvert\varepsilon_1\rvert$	$\lvert\varepsilon_{11}\rvert$	$\lvert\varepsilon_{13}\rvert$	$\lvert\varepsilon_1\rvert$	$\lvert\varepsilon_{11}\rvert$	$\lvert\varepsilon_{13}\rvert$
6	4.02	18.83	28.81	0.28	0.64	0.28
7	2.06	18.45	19.786	0.22	0.2	0.7
8	1.03	11.83	19.85	0.76	0.78	0.68
9	2.7	16.9	20.13	0.2	0.62	0.68
10	2.1	12.236	16.324	0.22	0.62	0.7

Table 3-4 The summarization of the average harmonic error at each

approximated polynomial orders.

Orders u	6	7	8	9	10
$\lvert\varepsilon_{1(avg)}\rvert$(%)	1.64	0.76	0.34	0.43	0.42
$\lvert\varepsilon_{11(avg)}\rvert$(%)	8.28	8.68	8.60	8.15	6.75
$\lvert\varepsilon_{13(avg)}\rvert$(%)	12.15	10.09	9.69	8.46	8.08

Obviously, the minimum fundamental error occurs at orders of 8, and the minimum error of 11_{th} and 13_{th} harmonics occurs at orders of 10. This table can be a reference for users to select adequate orders depending on the system demand. However, the accuracy may be not enough in some application requiring higher power quality. Another approach is illustrated in next section.

3.5.3 Error Analysis of the piecewise continuous 2-order polynomial approximation

A better approach is dividing the solution curves into several segments and, then, each segment is fitted by a 2-order polynomial. Because each 2-order polynomial is a parabola, we then divide the exact solution trajectory into several parabola segments and find the approximated 2-order equation for each segment in terms of the modulation index m_1 by curve-fitting method respectively. Thus, regardless of m_1, only 3 addition and 5 multiplication operations are involved in the calculation of each solution angle. For a better accuracy, each exact solution curves are divided into 12 segments. The values of the ending points and the coefficients of each parabola segment

corresponding to each solution trajectory are summarized in Table 3-5 to Table 3-10. The start point and the break point of the selected segment have a significant effect on the error caused by deviation. It can be observed that the harmonic error rises at the break point between two parabola segments. But the harmonic error in this case has been obviously attenuated compared with high order polynomial approximation. The relationship between the exact data points and the approximated parabola segments are shown in Fig. 3-16. The harmonic error analyses are shown in Fig. 3-17 as well.

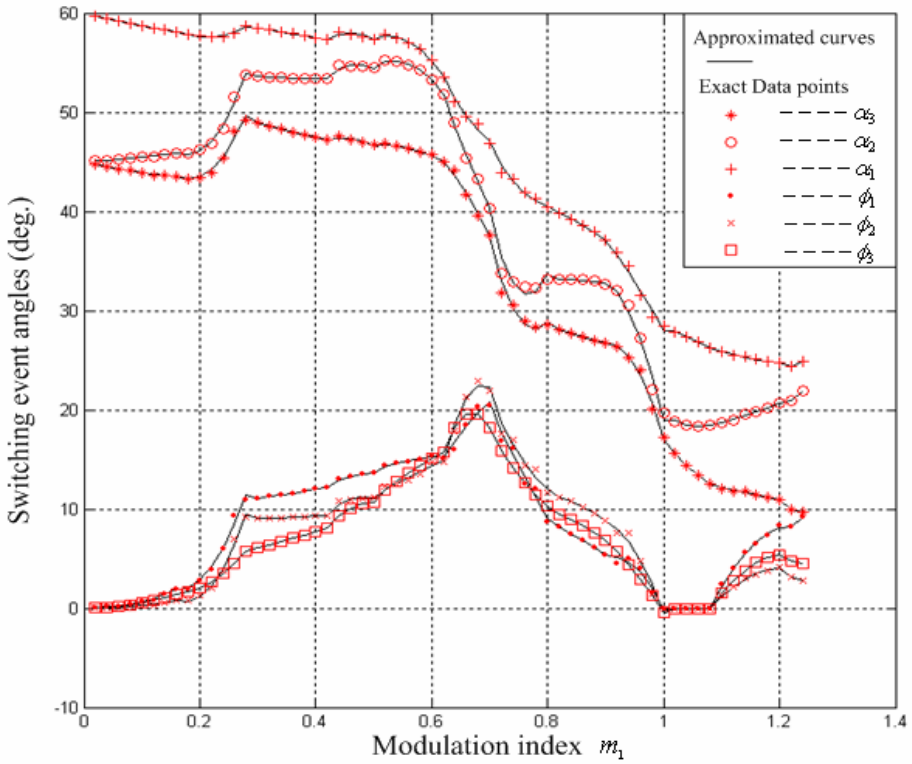

Fig. 3-16 The relationship between the exact data points and the approximated parabola segments.

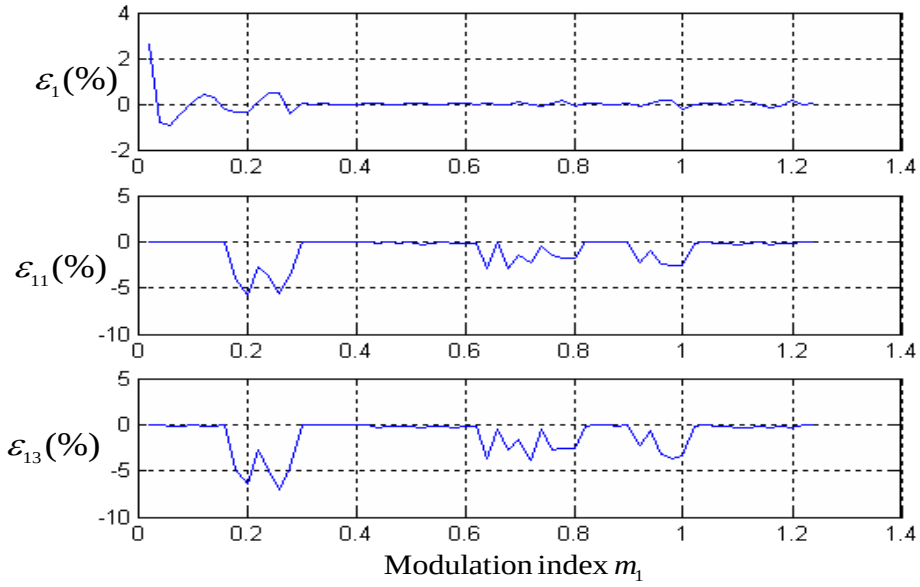

Fig. 3-17 The harmonic error ε_h derived from solutions between exact solutions and the approximated parabola segments.

Table 3-5 Approximated polynomial of each segment describing α_1.

Modulation index m_1	Polynomials describing α_1
0.02-0.16	$\alpha_1(m_1) = 36.83m_1^2 - 15.647m_1 + 45.095$
0.16-0.28	$\alpha_1(m_1) = 653.78m_1^2 - 236.57m_1 + 64.622$
0.28-0.42	$\alpha_1(m_1) = 8.32m_1^2 - 20.33m_1 + 54.26$
0.42-0.5	$\alpha_1(m_1) = -222.32m_1^2 - 197.05m_1 + 3.72$
0.5-0.62	$\alpha_1(m_1) = -137.62m_1^2 - 139.55m_1 + 11.4$
0.62-0.7	$\alpha_1(m_1) = -331.43m_1^2 + 341.27m_1 - 38.992$
0.7-0.8	$\alpha_1(m_1) = 1470.9m_1^2 - 2288.1m_1 + 917.93$
0.8-0.9	$\alpha_1(m_1) = 35.804m_1^2 - 79.017m_1 + 68.834$
0.9-1	$\alpha_1(m_1) = -1081.2m_1^2 + 1957.8m_1 - 859.58$
1-1.08	$\alpha_1(m_1) = 310m_1^2 - 702.29m_1 + 409.48$
1.08-1.2	$\alpha_1(m_1) = 18.929m_1^2 - 55.65m_1 + 50.488$
1.2-1.24	$\alpha_1(m_1) = 866.75m_1^2 - 2145.3m_1 + 1337.1$

Table 3-6 Approximated polynomial of each segment describing α_2.

Modulation index m_1	Polynomials describing α_2
0.02-0.16	$\alpha_2(m_1)=17.813m_1^2+2.23m_1+45.05$
0.16-0.28	$\alpha_2(m_1)=801.04m_1^2-286.67m_1+71.362$
0.28-0.42	$\alpha_2(m_1)=18.438m_1^2-14.95m_1+56.443$
0.42-0.5	$\alpha_2(m_1)=-496.07m_1^2+466.82m_1-54.989$
0.5-0.62	$\alpha_2(m_1)=-470.39m_1^2+503.58m_1-79.588$
0.62-0.7	$\alpha_2(m_1)=191.61m_1^2-396.3m_1+223.85$
0.7-0.8	$\alpha_2(m_1)=1783.3m_1^2-2732.2m_1+1078.1$
0.8-0.9	$\alpha_2(m_1)=-75.223m_1^2+123.66m_1-14.634$
0.9-1	$\alpha_2(m_1)=-1024.4m_1^2+1806.1m_1-762.71$
1-1.08	$\alpha_2(m_1)=366.07m_1^2-776.87m_1+430.47$
1.08-1.2	$\alpha_2(m_1)=24.583m_1^2-36.754m_1+29.386$
1.2-1.24	$\alpha_2(m_1)=908.75m_1^2-2185.6m_1+1334.8$

Table 3-7 Approximated polynomial of each segment describing α_3.

Modulation index m_1	Polynomials describing α_2
0.02-0.16	$\alpha_3(m_1)=14.643m_1^2-14.577m_1+60.038$
0.16-0.28	$\alpha_3(m_1)=227.35m_1^2-96.433m_1+67.772$
0.28-0.42	$\alpha_3(m_1)=6.265m_1^2-14.166m_1+62.188$
0.42-0.5	$\alpha_3(m_1)=-371.61m_1^2+339.93m_1-19.768$
0.5-0.62	$\alpha_3(m_1)=-441.55m_1^2+462.65m_1-63.494$
0.62-0.7	$\alpha_3(m_1)=354.29m_1^2-545.54m_1+255.4$
0.7-0.8	$\alpha_3(m_1)=462.72m_1^2-753.53m_1+347.26$
0.8-0.9	$\alpha_2(m_1)=-88.75m_1^2+118.33m_1+2.49$
0.9-1	$\alpha_3(m_1)=-77.455m_1^2+53.154m_1+52.303$
1-1.08	$\alpha_3(m_1)=13.75m_1^2-56.495m_1+71.228$
1.08-1.2	$\alpha_3(m_1)=44.554m_1^2-114.22m_1+97.603$
1.2-1.24	$\alpha_3(m_1)=1001.2m_1^2-2440m_1+1510.9$

Table 3-8 Approximated polynomial of each segment describing ϕ_1.

Modulation index m_1	Polynomials describing ϕ_1
0.02-0.16	$\phi_1(m_1) = 100.68m_1^2 - 5.69m_1 + 0.197$
0.16-0.28	$\phi_1(m_1) = 653.65m_1^2 - 207.14m_1 + 18.135$
0.28-0.42	$\phi_1(m_1) = 7.4m_1^2 - 4.06m_1 + 9.18$
0.42-0.5	$\phi_1(m_1) = -232.14m_1^2 + 230.39m_1 - 43.548$
0.5-0.62	$\phi_1(m_1) = -120.33m_1^2 + 147.08m_1 - 29.729$
0.62-0.7	$\phi_1(m_1) = -341.79m_1^2 + 525.77m_1 - 179.79$
0.7-0.8	$\phi_1(m_1) = 97.232m_1^2 - 255.31m_1 + 151.15$
0.8-0.9	$\phi_1(m_1) = -50.388m_1^2 + 51.507m_1 - 0.2015$
0.9-1	$\phi_1(m_1) = -677.96m_1^2 + 1235.8m_1 - 557.94$
1-1.08	$\phi_1(m_1) = 0$
1.08-1.2	$\phi_1(m_1) = -373.79m_1^2 + 919.02m_1 - 556.44$
1.2-1.24	$\phi_1(m_1) = 1282.1m_1^2 - 3105.6m_1 + 1888.7$

Table 3-9 Approximated polynomial of each segment describing ϕ_2.

Modulation index m_1	Polynomials describing ϕ_2
0.02-0.16	$\phi_2(m_1) = 47.064m_1^2 - 3.088m_1 + 0.0986$
0.16-0.28	$\phi_2(m_1) = 806.49m_1^2 - 283.87m_1 + 25.66$
0.28-0.42	$\phi_2(m_1) = 26.329m_1^2 - 17.054m_1 + 11.875$
0.42-0.5	$\phi_2(m_1) = -457.79m_1^2 + 439.93m_1 - 94.506$
0.5-0.62	$\phi_2(m_1) = -19.464m_1^2 + 51.718m_1 - 9.682$
0.62-0.7	$\phi_2(m_1) = -1730.2m_1^2 + 2380.4m_1 - 796.28$
0.7-0.8	$\phi_2(m_1) = 491.38m_1^2 - 830.09m_1 + 361.68$
0.8-0.9	$\phi_2(m_1) = -118.7m_1^2 + 173.76m_1 - 51.434$
0.9-1	$\phi_2(m_1) = -661.43m_1^2 + 1163.1m_1 - 502.22$
1-1.08	$\phi_2(m_1) = 0$
1.08-1.2	$\phi_2(m_1) = -248.03m_1^2 + 598.78m_1 - 357.34$
1.2-1.24	$\phi_2(m_1) = 642.37m_1^2 - 1599.6m_1 + 998.58$

Table 3-10 Approximated polynomial of each segment describing ϕ_3.

Modulation index m_1	Polynomials describing ϕ_3
0.02-0.16	$\phi_3(m_1) = 74.311m_1^2 - 3.56m_1 + 0.1363$
0.16-0.28	$\phi_3(m_1) = 264.71m_1^2 - 80.599m_1 + 7.5681$
0.28-0.42	$\phi_3(m_1) = 12.458m_1^2 + 7.634m_1 + 2.688$
0.42-0.5	$\phi_3(m_1) = -390.96m_1^2 + 389.93m_1 - 86.581$
0.5-0.62	$\phi_3(m_1) = -84.405m_1^2 + 134.75m_1 - 35.366$
0.62-0.7	$\phi_3(m_1) = -1658.9m_1^2 + 2221.9m_1 - 724.31$
0.7-0.8	$\phi_3(m_1) = 258.08m_1^2 - 461.91m_1 + 214.64$
0.8-0.9	$\phi_3(m_1) = -103.58m_1^2 + 144.74m_1 - 39.539$
0.9-1	$\phi_3(m_1) = -139.34m_1^2 + 191.06m_1 - 52.118$
1-1.08	$\phi_3(m_1) = 0$
1.08-1.2	$\phi_3(m_1) = -303.4m_1^2 + 736.14m_1 - 441.08$
1.2-1.24	$\phi_3(m_1) = 584.87m_1^2 - 1452.6m_1 + 906.39$

Chapter4 Hardware configuration and software programming

4.1 Introduction

Fig. 4-1 shows the diagram of system including the dc source, the two inverters, the zig-zag connected transformers, the output filter and the digital controller. The digital controller, based-on TMS320LF2812 (DSP) is in charge of the on-line calculation of the optimized switching angles through the approximated polynomials, the generation and management of triggered signals for the inverters' switches and executing the output voltage compensation. In addition to the DSP, this chapter also describes the peripheral circuits including voltage sensor circuit and the gate driver circuits. The program designing with flow charts will be detailed as well. The experiment has finished the whole range of route B from modulation index of 0.02 to 1.24.

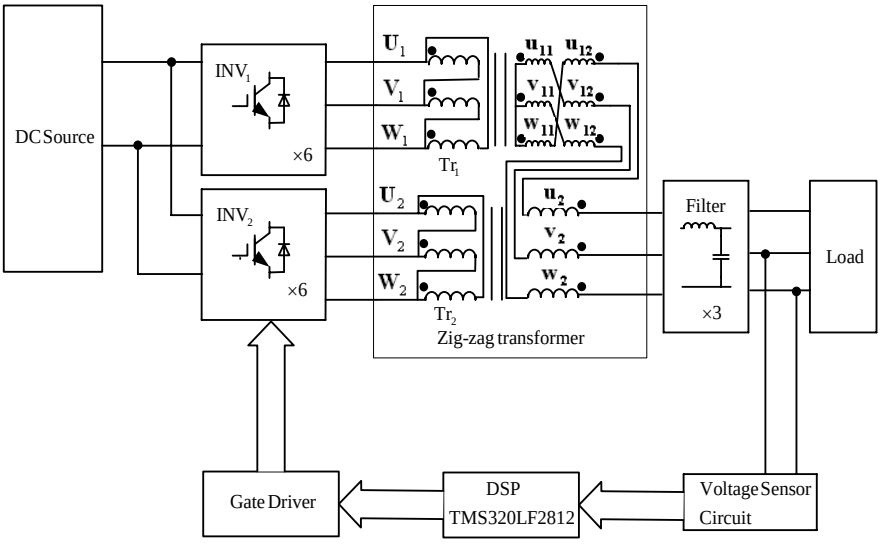

Fig. 4-1 The diagram of the proposal system.

4.2 Hardware description

This section introduces the hardware used in the thesis as abbreviate and clear as possible, which includes digital signal controller, inverter-related circuits and the voltage sensor circuit.

4.2.1 Digital signal processor (TMS320LF2812)

For practical implementation, the digital signal processor TMS320LF2812 is chose to realize the system controller because its high performance. The following describes the main features of this chip:

1. 150MIPS operation speed
2. On-chip memory
   (a) Flash Devices: Up to 128$k\times16$ flash (four 8$k\times16$ and six 16$k\times16$ sectors)
   (b) ROM devices: Up to 128$k\times16$ ROM
3. 16 channels' 12-Bit A/D converter
   (a) 2×8 channel input multiplexer
   (b) Two sample-and-hold circuits
   (c) Single/Simultaneous conversions
   (d) Fast conversion rate: 80 ns/ 12.5 MSPS
4. Three 32-Bit CPU-timers
5. Watchdog timer
6. Serial Peripheral Interface (SPI) and Serial Communications Interface (SCIA/SCIB)
7. Event Managers A and B
   (a) General-Purpose (GP) Timer
   (b) Compare-unit and 16 channels' PWM
   (c) Six Capture-unit and two QEP circuits

8. Up to 56 general purpose I/O (GPIO) pins
9. Three external interrupts

4.2.2 Inverter-related devices and peripheral circuits

This section describes the types and specifications of all devices employed in this inverter system. Some peripheral circuits are also introduced in this section respectively.

1. Switch device:

The inverters in this system use the IGBT switches (IXGH24N60CD1) manufactured by IXYS as shown in Fig. 4-2. The maximum switching time $t_{d(off)}$ is only 140 ns and it can suffer the maximum voltage difference V_{CES} of 600 *Volt* and current I_{C25} of 48 *Ampere* at temperature of 25 degrees.

2. Zig-zag connected transformers:

The KVA and voltage rating of the two transformers, which conduct zig-zag connection, are 2*k*VA 240/138 and 2*k*VA 240/240 respectively.

3. Gate driver circuit:

Each switch in the full-bridge inverters is driven by DSP through an optocoupler IC HCPL-3120, which provides isolation between DSP and the power stage, manufactured by Agilent firm. Using optocoupler IC is for protecting the microcontroller. Fig. 4-3 shows the gate driver circuit diagram with current-limited resistances connected in series to both the input and output terminals, where R_1 is 510 Ohm and R_2 is 270 Ohm.

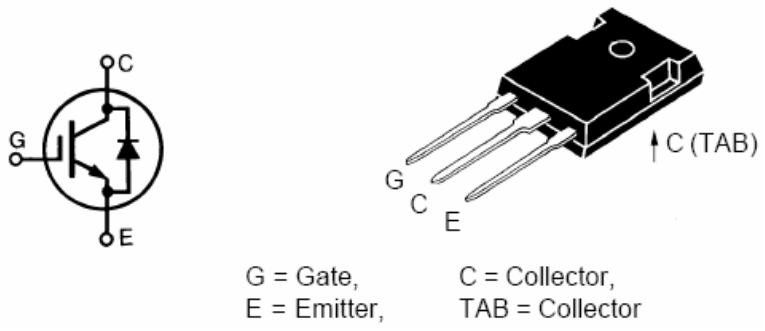

Fig. 4-2 The switch device IGBT IXGH24N60CD1

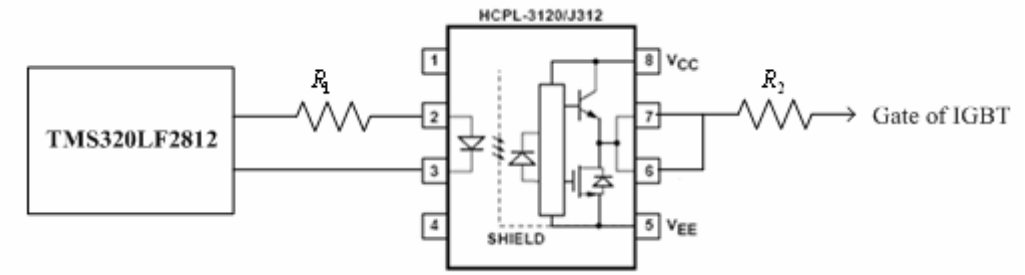

Fig. 4-3 The gate driver circuit HCPL-3120.

4. Output Filter:

This inverter system employs a 2-order three-phase filter to eliminate the harmonics equal or bigger than the 23-th and 25-th harmonics. The three-phase filter is connected between the zig-zag transformer output terminals and the load. The cut-off frequency is set at 375Hz by choosing L=1.5*m*H and C=40μF. Fig. 4-4 shows the filter structure.

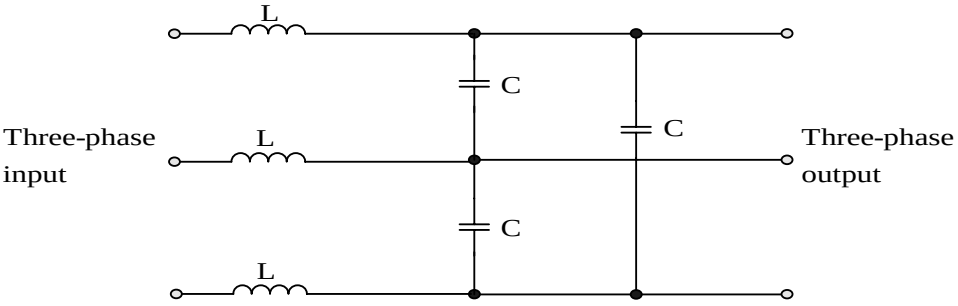

Fig. 4-4 The three-phase filter structure.

5. Voltage sensor circuit:

For implementing compensation of the output voltage, a voltage detect circuit is built by a voltage sensor LV-25P and two operational amplifiers (HA17741). As shown in Fig. 4-5, the output signal of the voltage sensor device is amplified by the first OPA with $-\frac{R_3}{R_2}$ voltage gain, then adjusted dc level by another OPA. The parameters of the circuit shown in Fig. 4-5 are as follow:

$R_1 : 50k\text{Ohm}$

$R_2, R_3 : 1k\text{Ohm}$

$R_4 - R_7 : 10k\text{Ohm}$

In order to get the peak voltage, the voltage sensor circuit is connected after a full-bridge filter model (RM15TB-H) and a big capacitance shown in Fig. 4-6.

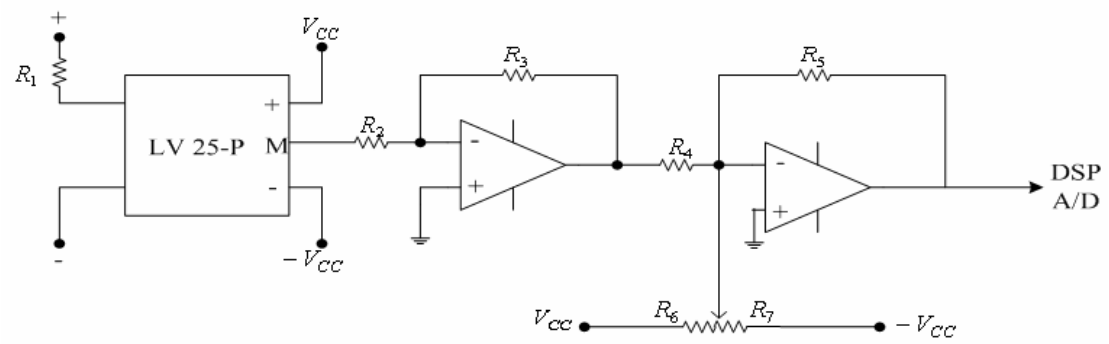

Fig. 4-5 The voltage sensor circuit diagram.

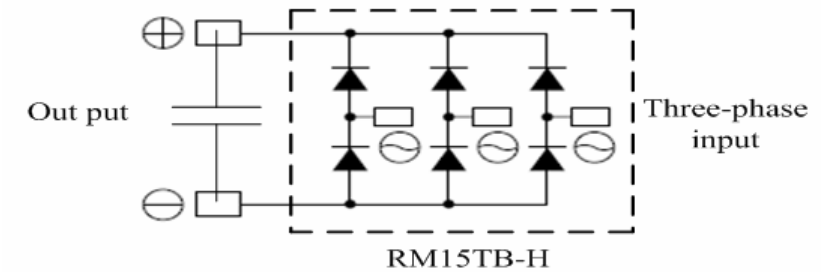

Fig. 4-6 Three-phase rectifier circuit.

4.3 Software programming

This section illustrates the flow charts of DSP programming and I/O port distribution. The code composer of the DSP is CCstudio V3.1 offered by the Texas Instrument (TI). Although both assembly language and C language can be used to code the program, the latter is chose for convenience. The interrupt events for PWM generation and on-line calculation will be detailed as well.

4.3.1 The I/O port pins and interrupts

According to the inverter structure, the DSP should send twelve triggered PWM signals in different phases and accept a feedback analogue signal. Although this chip offers 12 channels' PWM circuits, it's difficult to program twelve PWM waveforms in different phases in which the dead-band is involved. A better approach is using the general purpose I/O ports. TMS320LF2812 offers totally 56 GPIO pins which are divided into six groups GPIOA, GPIOB, GPIOD, GPIOE, GPIOF and GPIOG. GPIOA0 to GPIOA11 are deployed to trig the 12 IGBTs and the pins' distribution is summarized in table 4-1. In order to precisely control the waveforms and feedback calculation, four compare interrupts, summarized in Table 4-2, (T1CINT to T4CINT) are employed. Three of the interrupts are for PWM generation, and one for receiving the A/D data and on-line calculating the optimal switching angles.

Table 4-1 DSP pins' formulation

Pins	Connection
GPIOA0, GPIOA1	The first leg of Inverter 1, SU_1 and SU_1'
GPIOA2, GPIOA3	The second leg of Inverter 1, SV_1 and SV_1'
GPIOA4, GPIOA5	The third leg of Inverter 1, SW_1 and SW_1'
GPIOA6, GPIOA7	The first leg of Inverter 2, SU_2 and SU_2'
GPIOA8, GPIOA9	The second leg of Inverter 2, SV_2 and SV_2'
GPIOA10, GPIOA11	The third leg of Inverter 2, SW_2 and SW_2'
ADCINA0	Voltage sensor output

Table 4-2 Interrupt formulation

Interrupt category	Function
Timer1 compare interrupt (T1CNT)	Generating the triggered waveform of SU_1, SU_1', SV_1 and SV_1'
Timer2 compare interrupt (T2CNT)	Generating the triggered waveform of SW_1, SW_1', SU_2 and SU_2'
Timer3 compare interrupt (T3CNT)	Generating the triggered waveform of SV_2, SV_2', SW_2 and SW_2'
Timer4 compare interrupt (T4CNT)	Receiving the A/D data and on-line calculating the optimal switching angles

4.3.2 Voltage compensation processing

In order to perform the voltage compensation, the output voltage is detected through a voltage sensor circuit in which a rectifier model and a capacitor are employed. The A/D converter receives uni-polar voltage with the range from 0~3.3 *Volt* and transfers the input voltage to a 12-bit digital value. In this thesis, the maximum output voltage is set to 60 *Volt*, and the voltage sensor adapts this voltage to 3 *Volt*. The result digital value is given by

$$Digital\,value = 4095 \times \frac{Input\,voltage}{reference\,voltage} \tag{4-1}$$

where the reference voltage is 3.3 *Volt*, and input voltage is $\frac{V_{DC}}{20}$.

The digital value will be stored in ADCRESULT register for voltage compensation. If the output voltage is not equal to the desired value, it will be compensated by increasing or decreasing the modulation index.

4.3.3 Program designing with flow charts

The program includes the main program and the interrupt service routines. The program routine begins with setting the control register and defining the variables' type, then waiting for the interrupts occur in main program. The interrupt service routines manage controlling the triggered PWM signals and voltage compensation. Fig. 4-7 shows the flow charts of main program for better comprehension.

When satisfying the interrupt conditions, the program begins to execute the interrupt service routine. This thesis uses three compare interrupts service routine to control the switches, each for four switches. The values stored in T1CMPR, T2CMPR and T3CMPR register

determine the moment that the interrupt occurs. At the end of the interrupt service routine, the TxCMPR register will be reloaded.

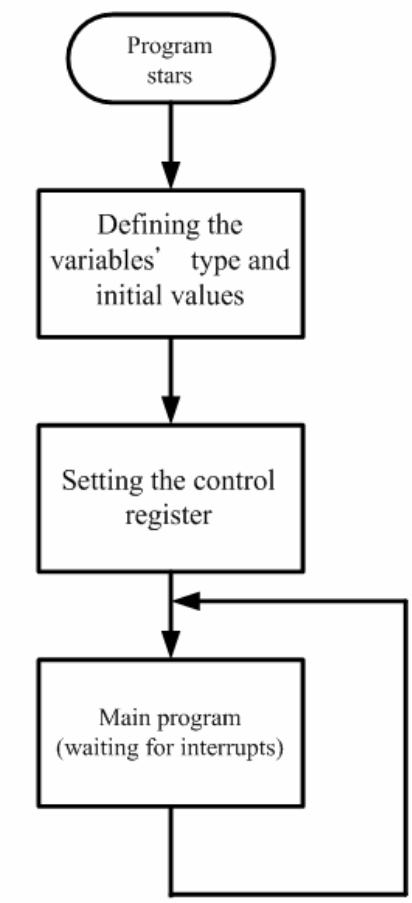

Fig. 4-7 The flow charts of main program.

Timer 4 Compare Interrupt (T4CINT) manages the feedback signal processing for voltage compensation. Before the program starts running, the initial switching angles should be set in advance. In this thesis, the program starts with the modulation index of 1.0. The fundamental magnitude of the PWM waveform will then be modulated to the desired value. The detail program routine is illustrated below.

1. PWM signal generation

Step1: Setting the initial value

The first step is to table the switching event angles for each phase. There are 14 switching events in one fundamental period and totally six phase-shifted identical waveforms need to generate, so this table contains 84 16-bit-integral data. The DSP system frequency is divided by 64 by setting the timer control register TxCON for convenience, and the result clock period is $0.43\mu s$. The timer period register, TxPR, is used to set the fundamental frequency and 39060 is for setting fundamental at 60 Hz. The interrupt occurs when timer counts up to the value of TxCMPR, therefore, the initial value of TxCMPR should be set to the first switching event. The switching event angles in terms of digital number are given by

$$Digital\ number = \frac{Deg.}{360} \times 39060 \qquad (4\text{-}2)$$

where the ‘‘Deg.’’ are the degrees of the switching event angles. The interrupt service routine changes the I/O port on/off state for the switches by changing I/O port states. Fig. 4-8 illustrates two identical PWM waveforms with 30 degrees phase difference as an example. Tri_1 and Tri_2 are two variable for determining when the switch state should be changed. Tri_1, first, stores the digital number of the first switching event $\alpha_1 + \phi_1$ in Phse1 PWM, and Tri_2 stores the digital number of the first switching event $\alpha_1 + \phi_1 + 30$ in Phase2 PWM. Then, the timer compare register TxCMPR stores the same value with Tri_1.

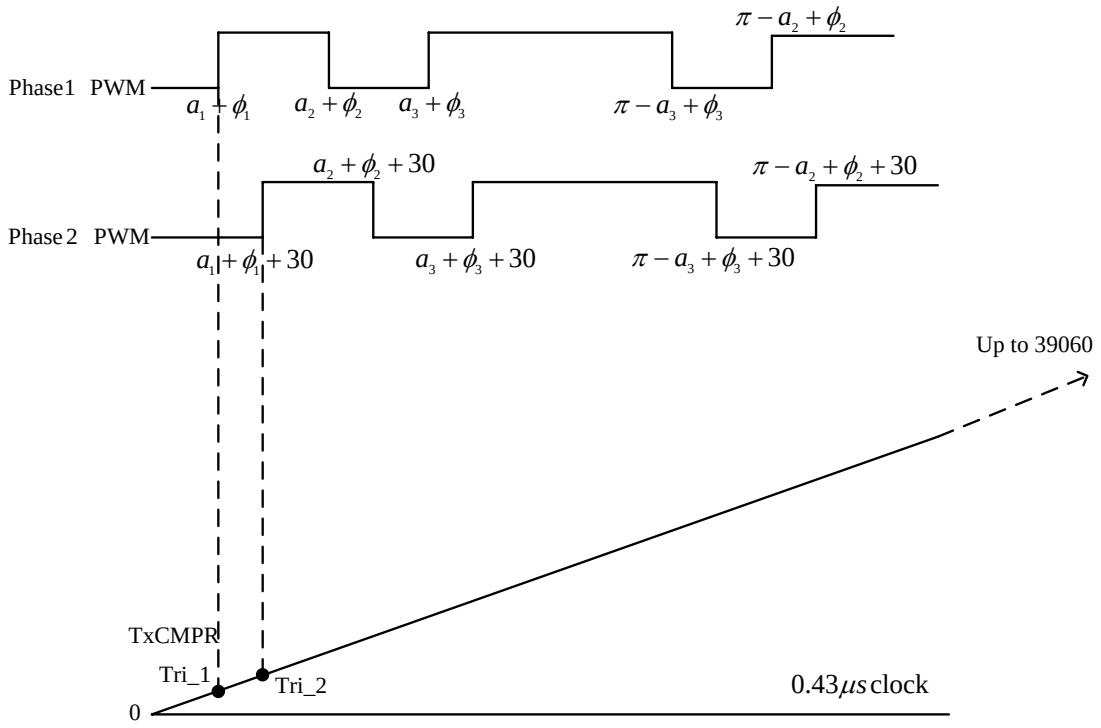

Fig. 4-8 Program illustration 1.

Step2: Interrupt event: Determining when the PWM state should be changed

When the clock counts up to the value stored in TxCMPR, the interrupt occurs. In the interrupt service routine, there is a conditional expression that, if T1CMPR equals to Tri_1, Phase1 PWM will change the state, and if T1CMPR equals to Tri_2, Phase2 PWM will change the state. After changing the Phase1 PWM state, the variable Tri_1 will be set to the next digital value of switching event angle as shown in Fig. 4-9.

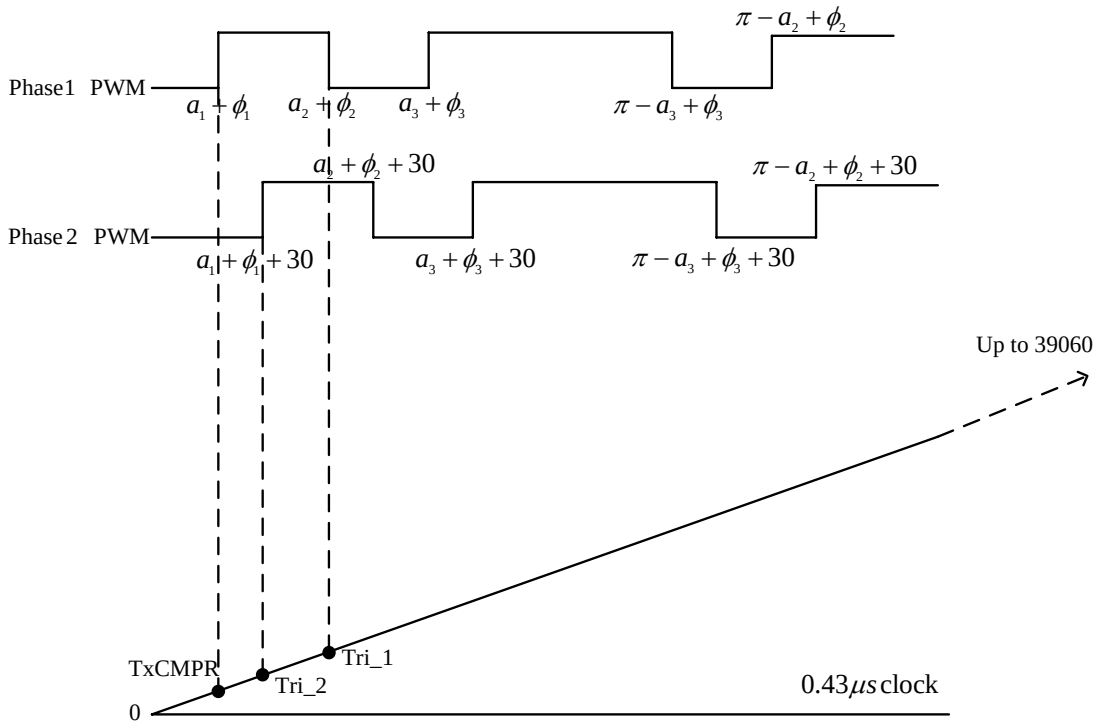

Fig. 4-9 Program illustration 2.

Step3: Deciding the next interrupt moment

Now, the two variables Tri_1 and Tri_2 and the register TxCMPR store different digital values. The next step is to determine the next interrupt moment. There are some conditional expressions to judge which variable, Tri_1 or Tri_2, are nearer to TxCMPR. TxCMPR will then be set to the value equal to the nearest variable (Tri_1 or Tri_2), because the nearest Tri_X value is the next interrupt-occurring point. This time, the register T1xCMPR will be set to the value equal to Tri_2 as shown in Fig. 4-10. Then, the interrupt service routine stops, waiting for next interrupt occurs. As the next interrupt occurs, the program routine is back to step2 again. Fig. 4-11 shows the flow charts of this program.

The advantage of this method for generating PWM waveform is, even the switching event angles are changed, the program is needless to

be revised. Therefore, adjusting the modulation index to control the fundamental magnitude is feasible in this program.

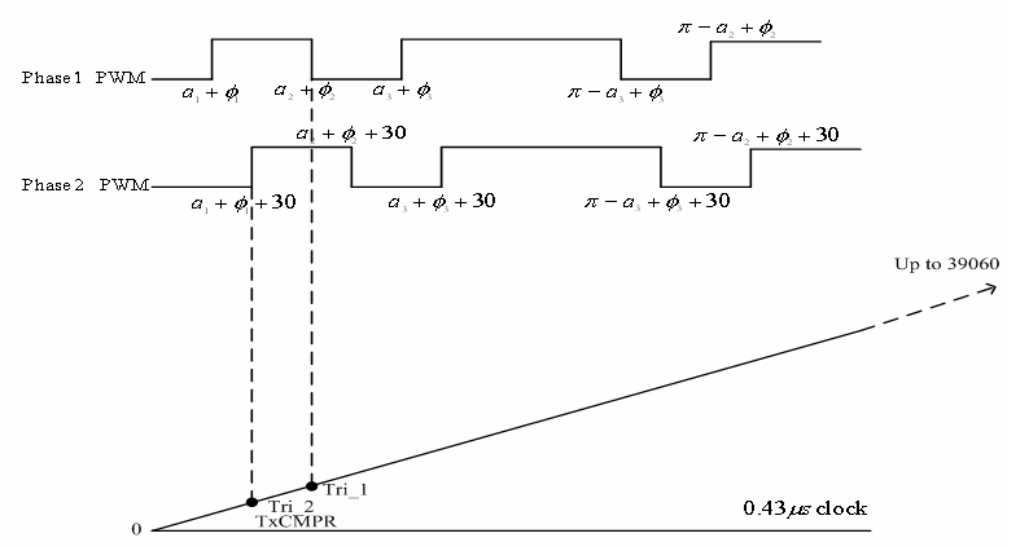

Fig. 4-10 Program illustration 3.

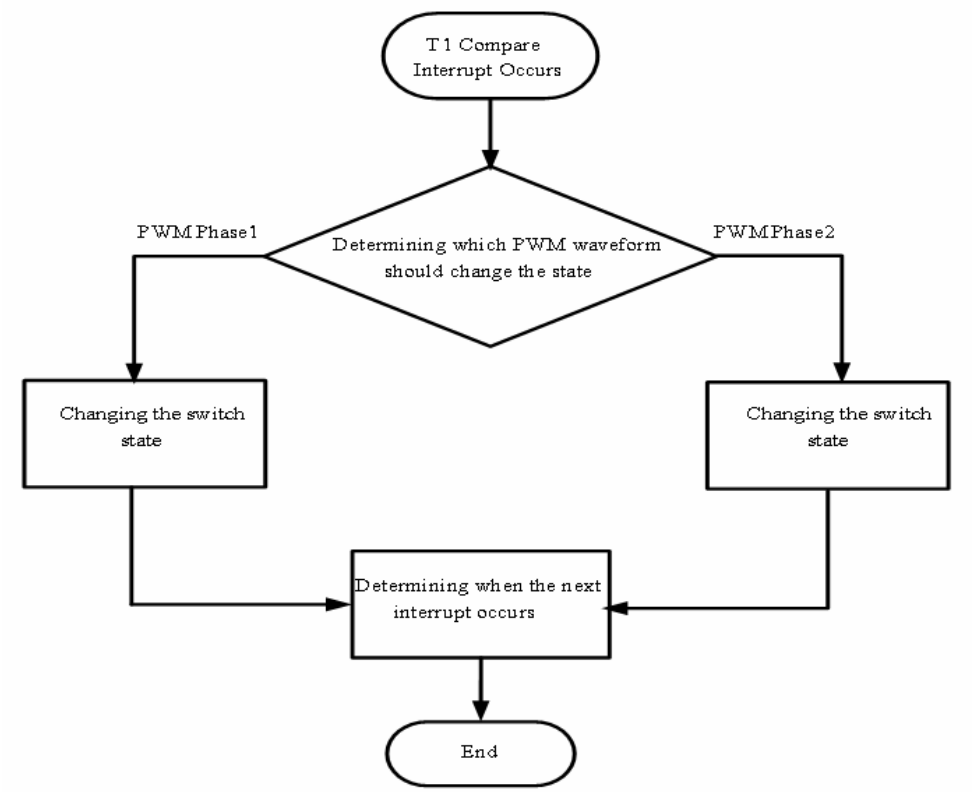

Fig. 4-11 Flow charts of timer1 interrupt service routine.

2. Voltage compensation processing

Timer4 compare interrupt manages the voltage compensation processing and the switching event angles' computing. The output voltage is detected through voltage sensor, then the A/D converter transfers the voltage to a digital value. After comparing with the desired voltage, the voltage compensation routine adjusts the old modulation index to a new one, then substitutes new m_1 in Table 3-5 to Table 3-9 to compute six new event angles α_1, α_2, α_3, ϕ_1, ϕ_2 and ϕ_3. Fig. 4-12 shows the flow charts of voltage compensation interrupt service routine.

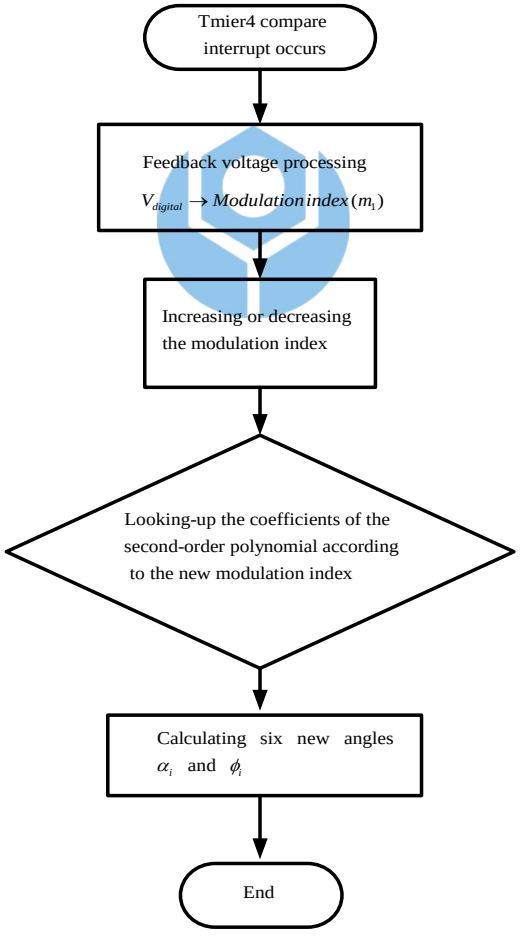

Fig. 4-12 Flow charts of timer4 interrupt service routine.

Chapter 5 Simulation and experimental results

5.1 Introduction

This chapter presents both the simulation and the experimental results to verify the validity of the proposed system. This thesis uses Matlab/Simulink to simulate the proposed system and employs TMS320LF2812 as the digital controller in the experiment.

5.2 Simulation of zig-zag transformers' output waveforms

Fig. 5-1 shows the simulation block diagrams of the proposed system, which is separated into six blocks. The following describes the function of each block respectively.

Block1:

This block is a programmable device with single input and six outputs and is implemented by S-Function in Matlab/Simulink. According to the input voltage command, Block1 manages calculating the variables α_i and ϕ_i, and substituting the variable u, in Table 3-5 to Table 3-9. The input command is given by the feedback circuit in Block6.

Block2:

Block2 models the two inverters and is also an S-Function. It has seven inputs, six angle data given by Block1 and a periodic value given by a waveform generator. According to these seven inputs, this block generates six voltages in different phases for zig-zag transformers inputs.

Block3:

This block is a scope for observing the waveforms generated from block2. Fig. 5-2 shows the six voltage waveforms for the transformers' inputs.

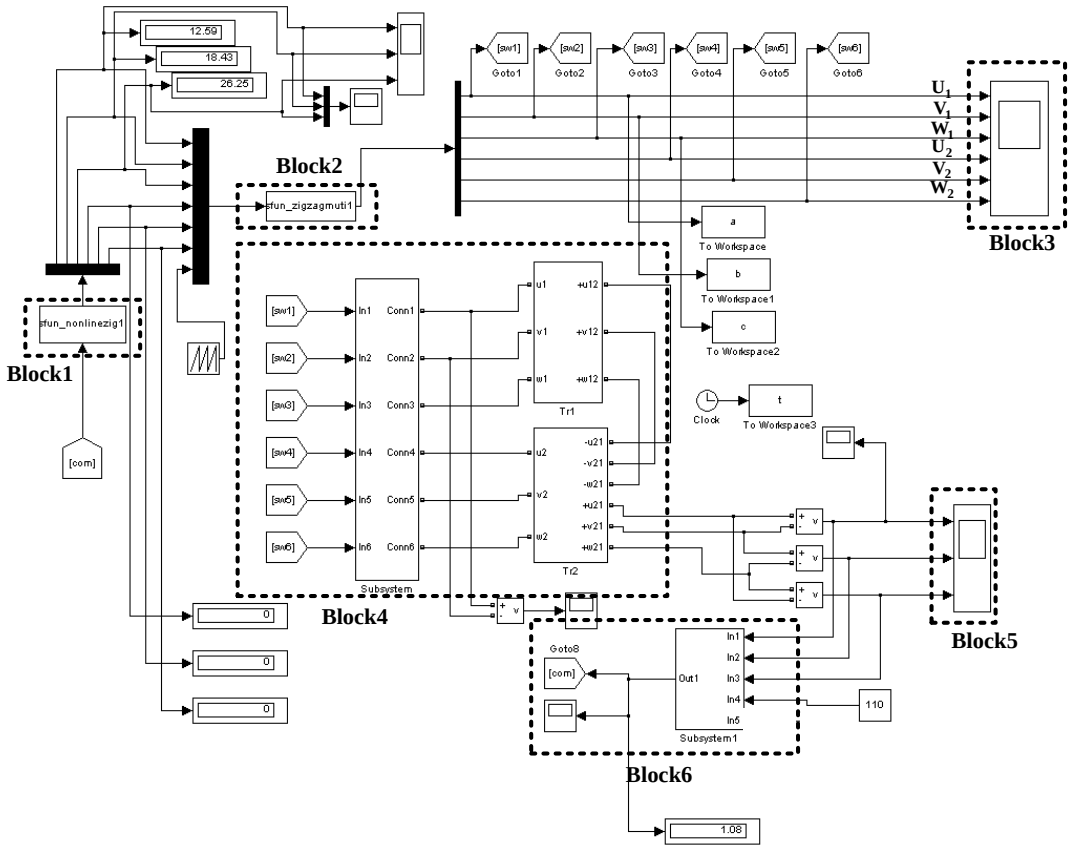

Fig. 5-1 Simulation block diagram of proposed system.

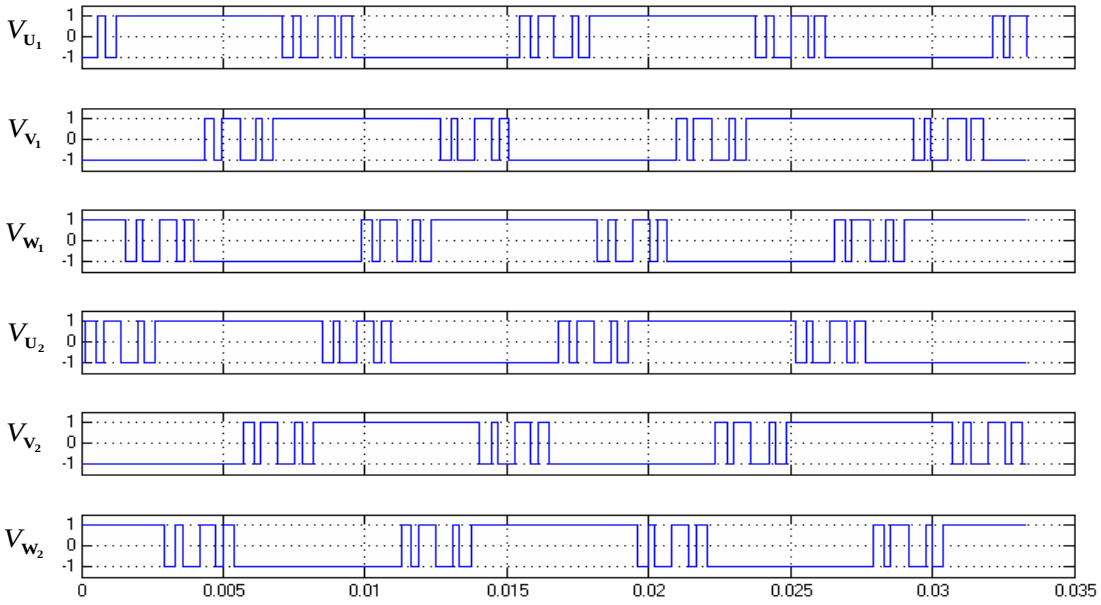

Fig. 5-2 Six voltage waveforms of transformers inputs.

Block4:

Block4 shows the simulation block of zig-zag transformers. Six PWM waveforms generated by Block2 are connected to the transformers inputs through six connection ports.

Block5:

This block is also a scope for observing the waveforms of transformers line-to-line outputs. Fig. 5-3 shows the three-phase-balanced outputs of this system. Two-level six phases' PWM inputs result in three 9-level line-to-line outputs.

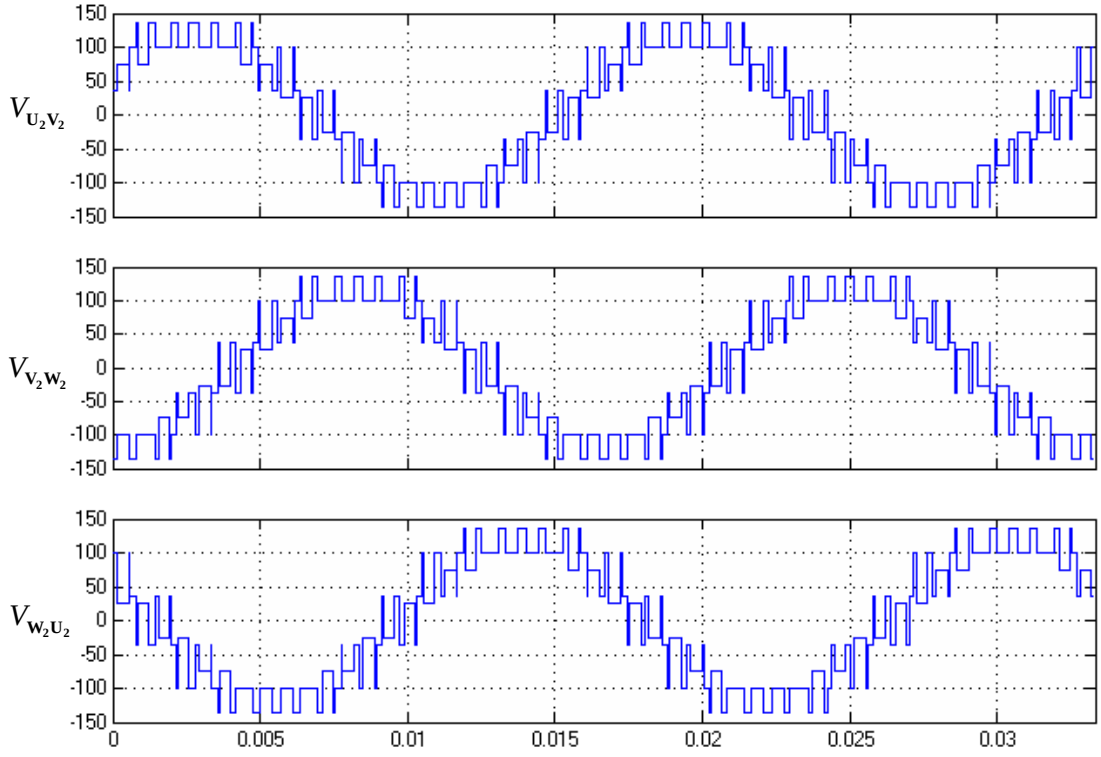

Fig. 5-3 Simulation result of zig-zag transformers three-phase line-to-line outputs.

Block6:

This block manages the feedback control of this system, which has four inputs and one output. Inputs In1, In2 and In3 are used to measure the three-phase outputs of the transformers. The desired output line-to-line voltage is set through In4, then this block determines the voltage command and supplies to Block1.

5.3 The simulation analyses and the experimental results

This section exhibits some selected experiment results with different modulation indexes and different fundamental phase shift, and the variation in 23-th and 25-th harmonics are used for comparison. The simulation results are demonstrated for contrast as well. Both simulated and experimental waveforms are analyzed by Matlab/Simulink FFT function to obtain their spectrums.

Fig. 5-4 shows the triggered waveforms for switches SU_1 and $SU_1^{'}$. A 10 μs dead time is set for each switching pair with complementary waveform. Fig. 5-5 shows the triggered waveforms, SU_1 and SU_2, in 30 degrees phase difference. Fig. 5-6 shows the triggered waveforms, SU_1 and SV_1, in 120 degrees phase difference. Both the 30 degrees and 120 degrees phase difference relations are for cooperating with the zig-zag connected transformers. Fig. 5-7 shows the inverter line-to-line waveforms $V_{U_1V_1}$ and $V_{U_2V_2}$ in 30 degrees phase difference, and Fig.5-8 shows the inverter line-to-line waveforms $V_{U_1V_1}$ and $V_{V_1W_1}$ in 120 degrees phase difference. Fig.5-9 shows the line-to-line waveforms of zig-zag transformers' output. All the waveforms from Fig. 5-4 to Fig. 5-9 are at

modulation index of 1.0 and $\gamma_1 = 12^\circ$, which provides the lowest 23-th and 25-th harmonics than other γ_1 at $m_1 =$ 1.0. Next, the following illustrates the variation in 23-th and 25-th harmonics from different fundamental phase shift.

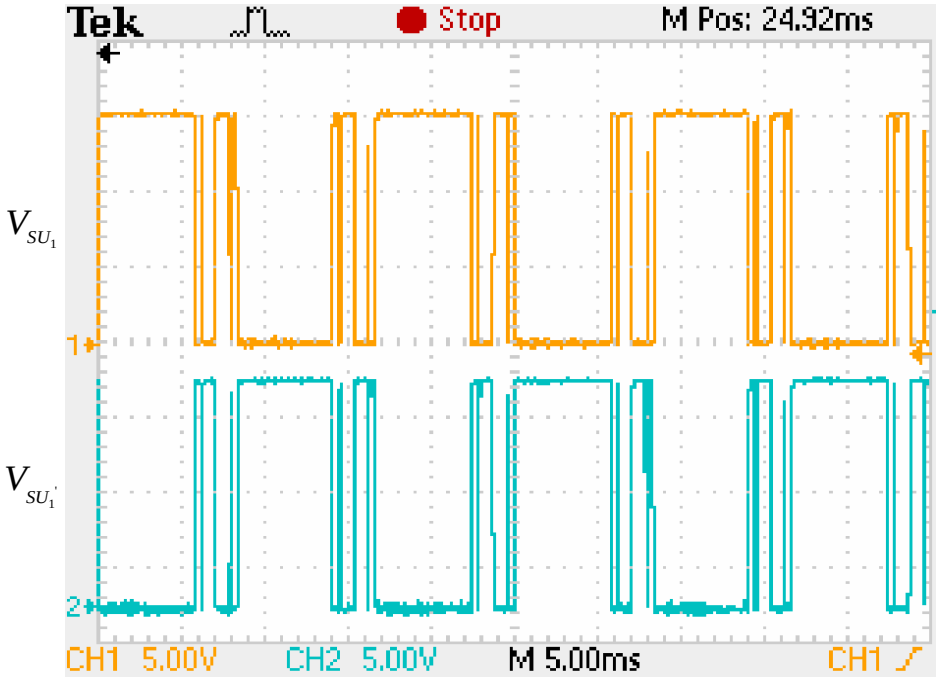

Fig.5-4 The triggered waveforms for switches in one leg at modulation index of 1 and $\gamma_1 = 12^\circ$ (5V/div, 5ms/div).

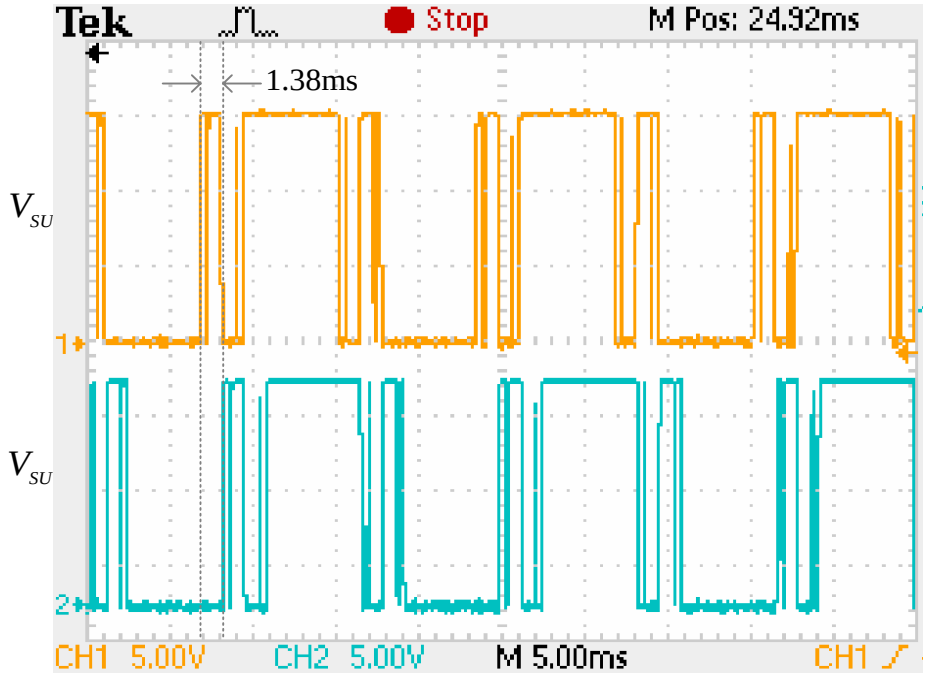

Fig.5-5 The triggered waveforms in 30 degrees phase difference for SU_1 and SU_2 at modulation index of 1.0 and $\gamma_1 = 12^\circ$ (5V/div, 5ms/div).

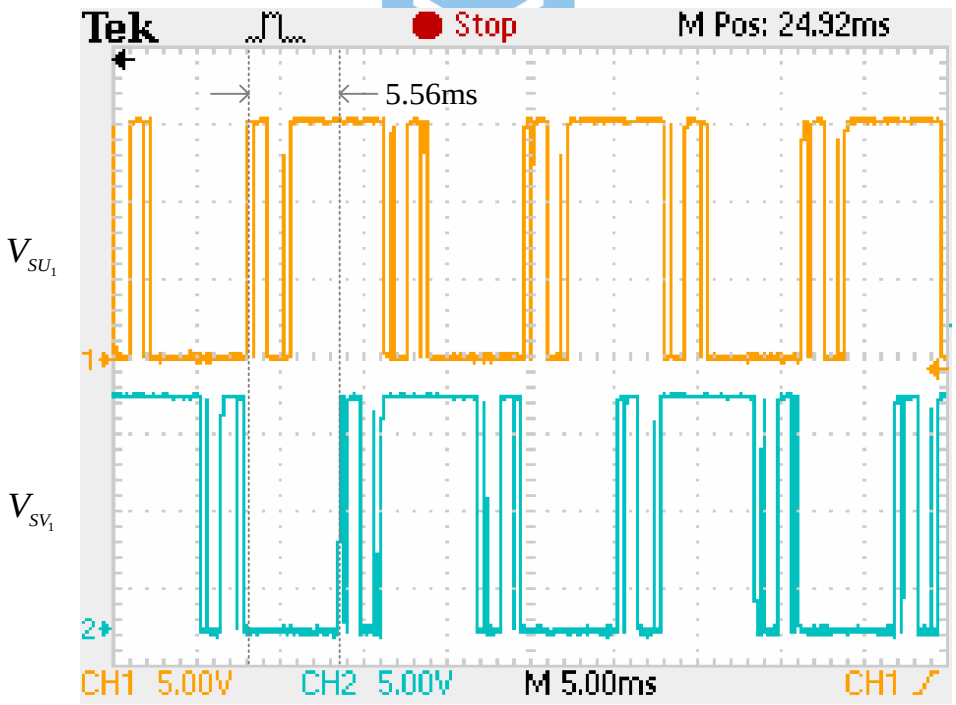

Fig.5-6 The triggered waveforms in 120 degrees phase difference for SU_1 and SV_1 at modulation index of 1.0 and $\gamma_1 = 12^\circ$ (5V/div, 5ms/div).

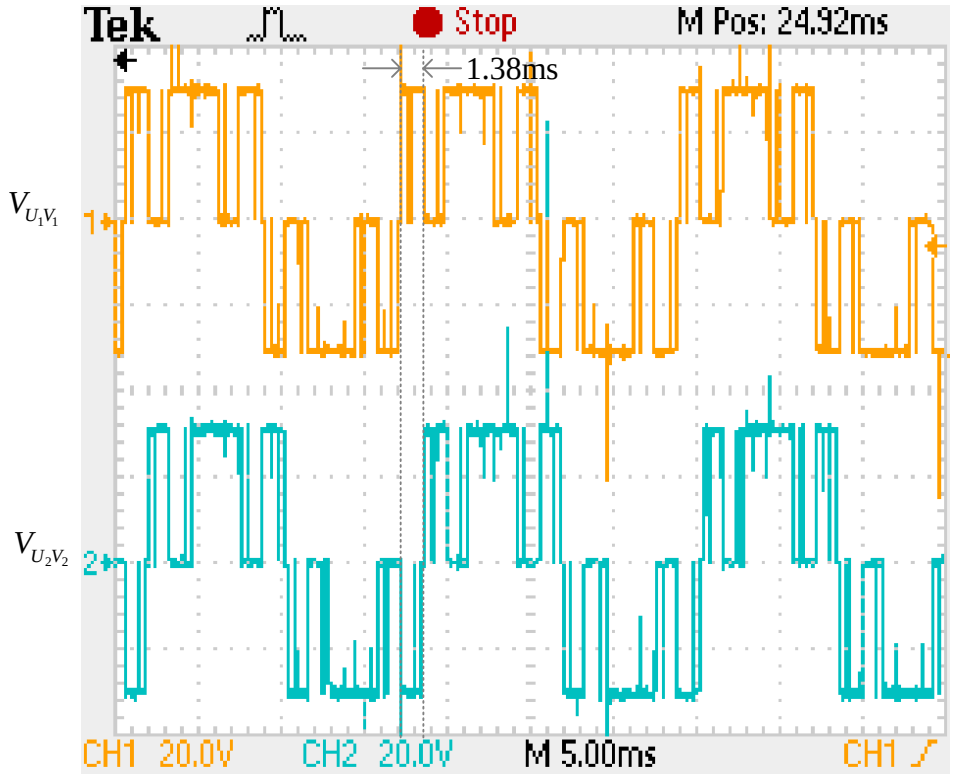

Fig.5-7 The inverter line-to-line waveforms in 30 degrees phase difference between $V_{U_1V_1}$ and $V_{U_2V_2}$ at modulation index of 1.0 and $\gamma_1 = 12^\circ$ (5V/div, 5ms/div).

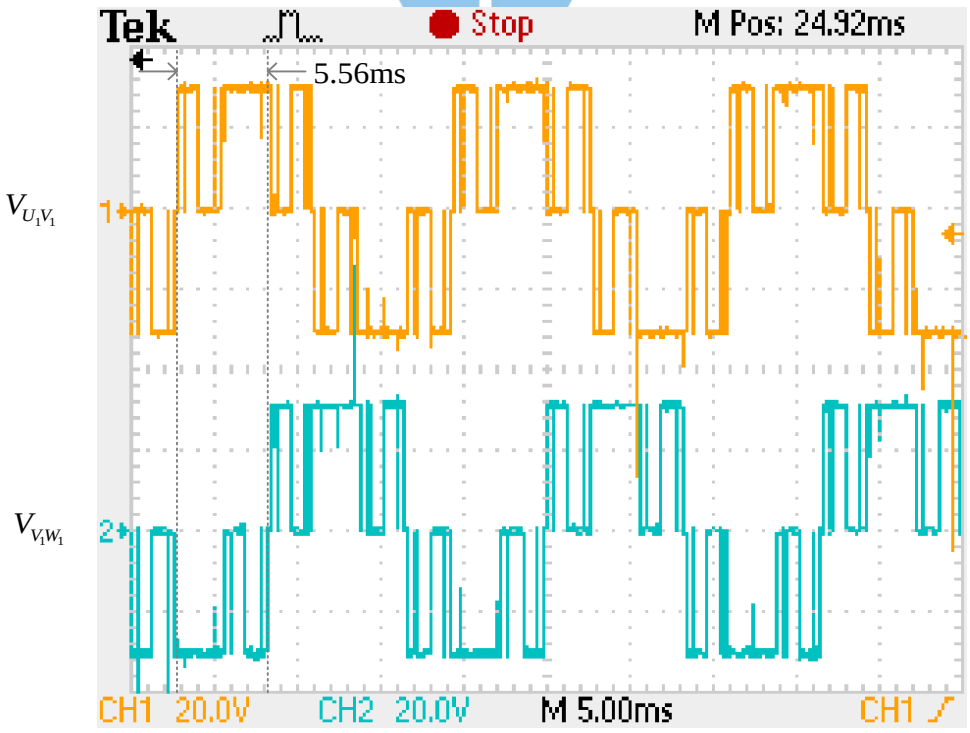

Fig.5-8 The inverter line-to-line waveforms in 120 degrees phase difference between $V_{U_1V_1}$ and $V_{V_1W_1}$ at modulation index of 1.0 and $\gamma_1 = 12^\circ$ (5V/div, 5ms/div).

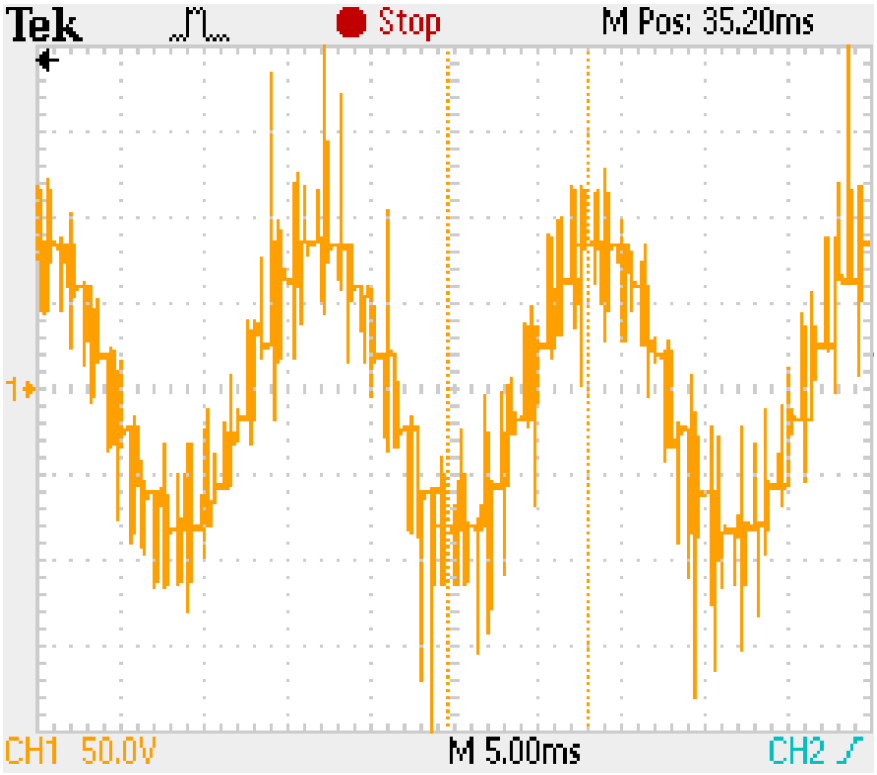

Fig.5-9 The line-to-line waveform of zig-zag output at modulation index of 1.0 and $\gamma_1 = 12^\circ$ (5V/div, 5ms/div).

Fig. 5-10(a) and Fig. 5-10(b) show the line-to-line waveforms and spectrums of simulated and experimental results at modulation index of 1.0 and $\gamma_1 = 12^\circ$. Fig. 5-11(a) and Fig. 5-11(b) show the same comparison at modulation index of 1.0 and $\gamma_1 = 0^\circ$. Although the 23-th harmonic of the waveform at $\gamma_1 = 12^\circ$ is larger than that in $\gamma_1 = 0^\circ$, the root sum square of the 23-th and 25-th harmonics for $\gamma_1 = 12^\circ$ is still smaller than the latter. The RSS (root sum square), in experimental result, of the waveform at $\gamma_1 = 12^\circ$ is 15.27V, and the RSS of the waveform at $\gamma_1 = 0^\circ$ is 15.93V.

The following illustrates another example that reduces the 23-th and 25-th harmonics much more obviously as changing the fundamental

phase γ_1. Fig. 5-12(a) and Fig. 5-12(b) show the simulated and experimental results of zig-zag transformers' output at modulation index of 0.5 and $\gamma_1 = 0^\circ$. Fig. 5-13(a) and Fig. 5-13(b) show the simulated and experimental results at modulation index of 0.5 and $\gamma_1 = 50^\circ$. The 23-th and 25-th harmonics are obviously reduced as γ_1 is shifted to 50 degrees, where the RSS of the 23-th and 25-th harmonics at $\gamma_1 = 0^\circ$ is 34.88V and 14.77V at $\gamma_1 = 50^\circ$. Fig.5-14 shows the experimental result of the filter output line-to-line voltage at modulation index of 0.5 and $\gamma_1 = 0^\circ$ in Fig.5-14(a), and $\gamma_1 = 50^\circ$ in Fig.5-14(b). The THD decreases from 2.05% to 0.91%. Fig. 5-15 shows the THD of the filter output waveform of Route B ranging from modulation index of 0.02 to 1.24. Apparently the THD decreases as the modulation index increases.

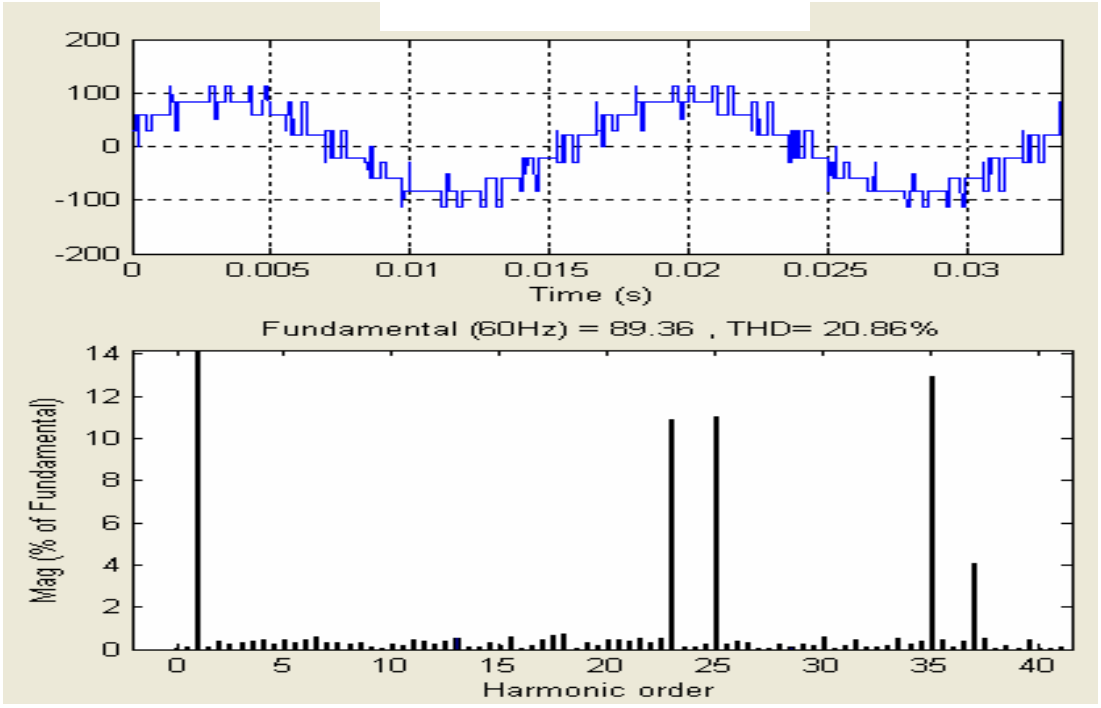

(a)

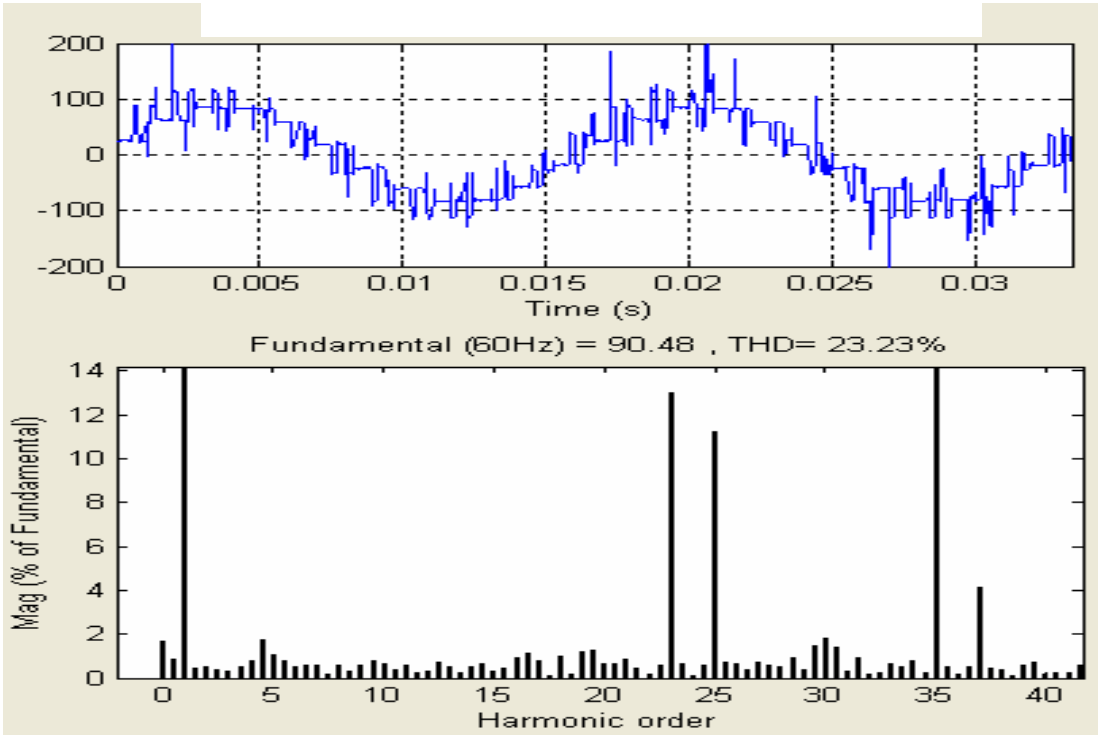

(b)

Fig.5-10 FFT analysis of the (a) simulated and (b) experimental line-to-line waveform of zig-zag output at modulation index of 1.0 and $\gamma_1 = 0^\circ$.

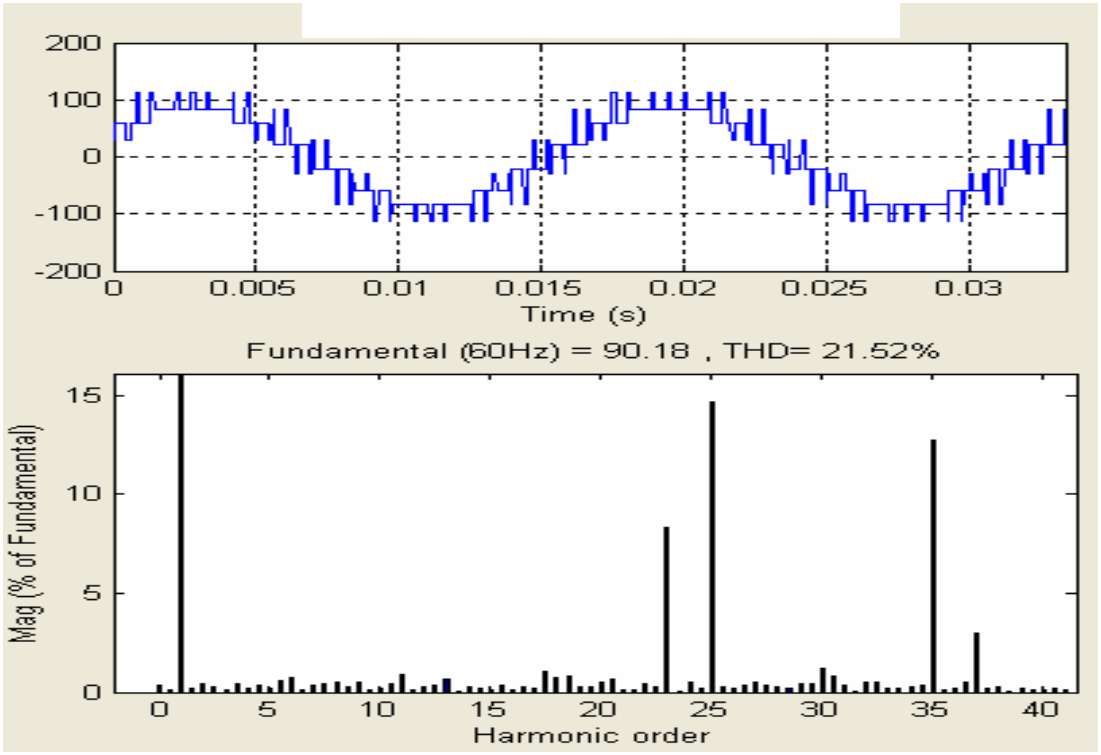

(a)

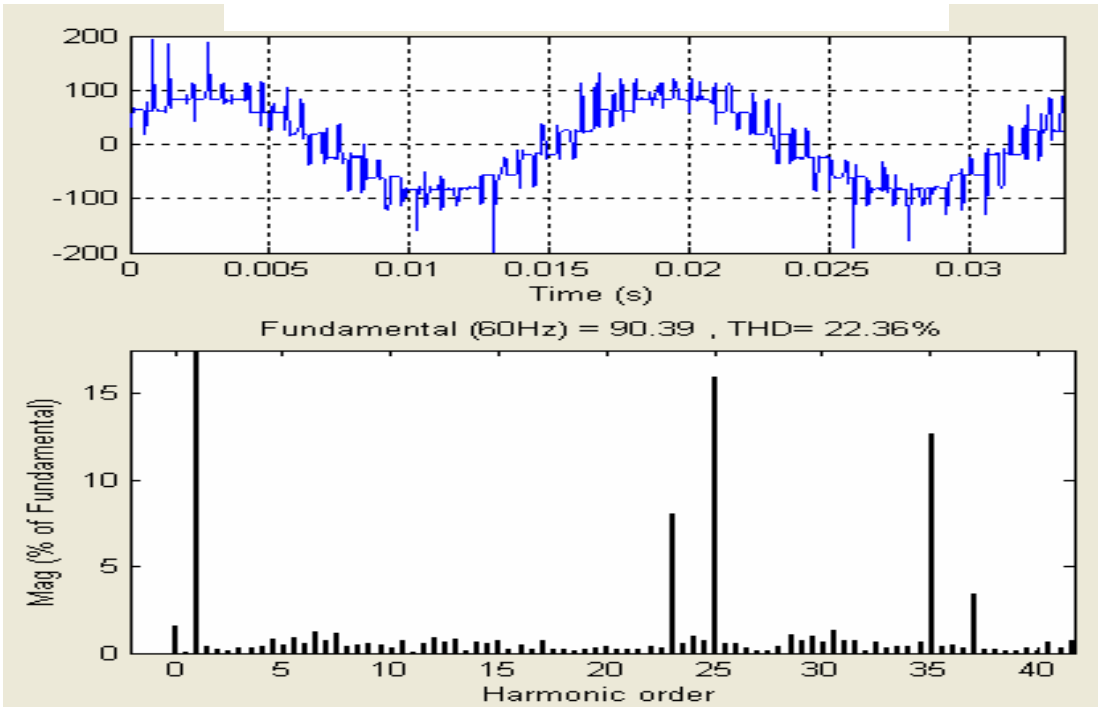

(b)

Fig.5-11 FFT analysis of the (a) simulated and (b) experimental line-to-line waveform of zig-zag output at modulation index of 1.0 and $\gamma_1 = 12^\circ$.

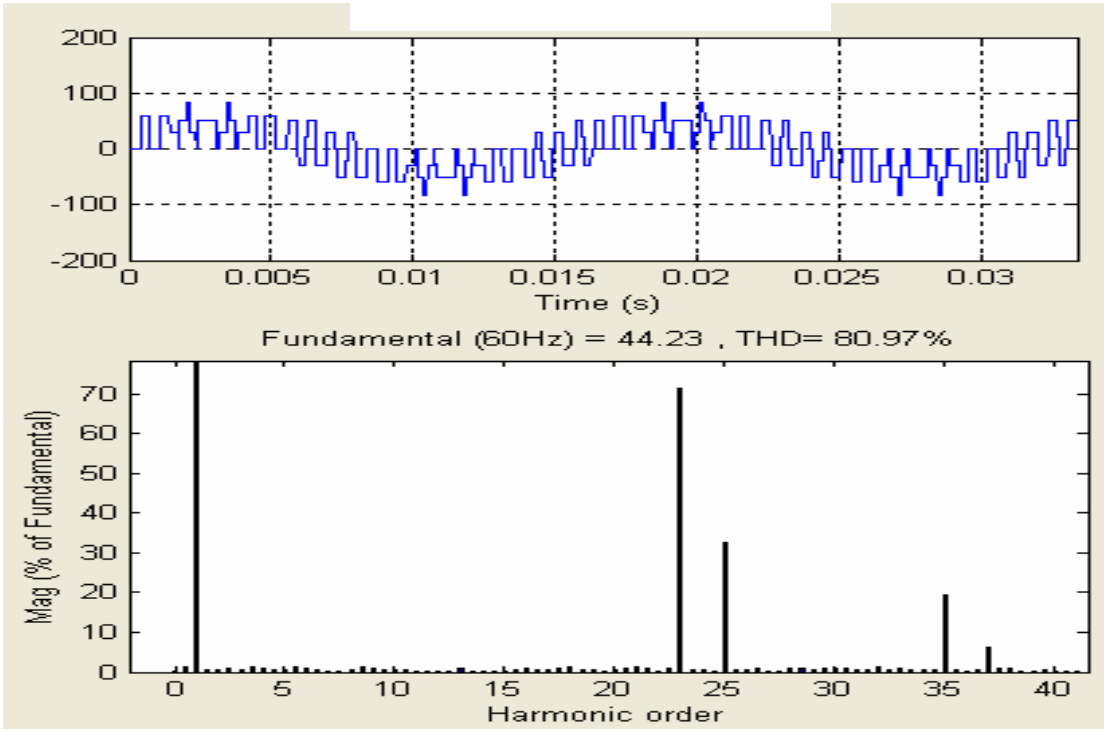

(a)

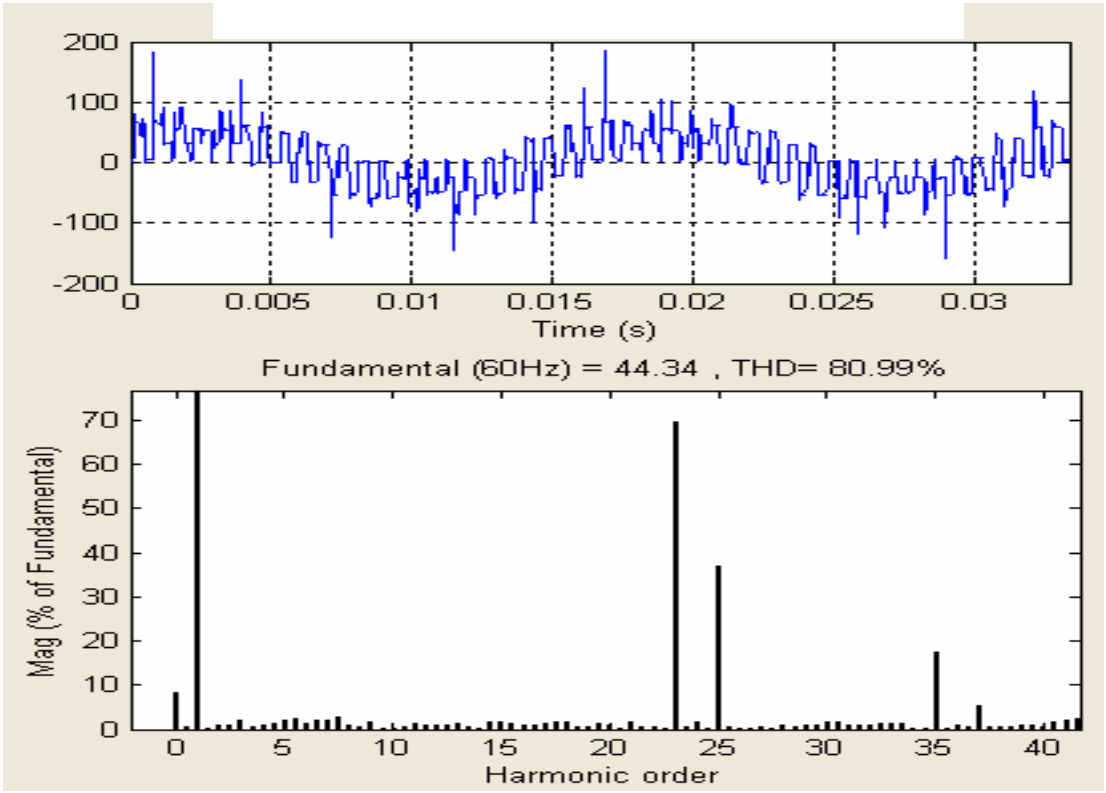

(b)

Fig.5-12 FFT analysis of the (a) simulated and (b) experimental line-to-line waveform of zig-zag output at modulation index of 0.5 and $\gamma_1 = 0^\circ$.

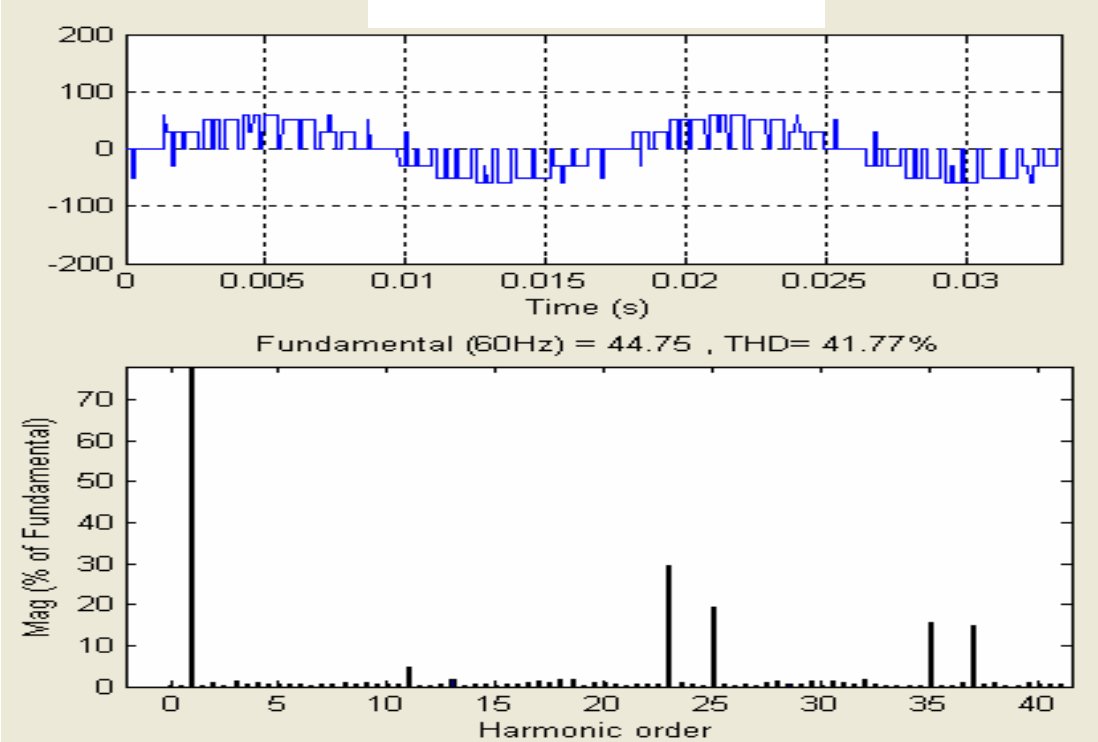

(a)

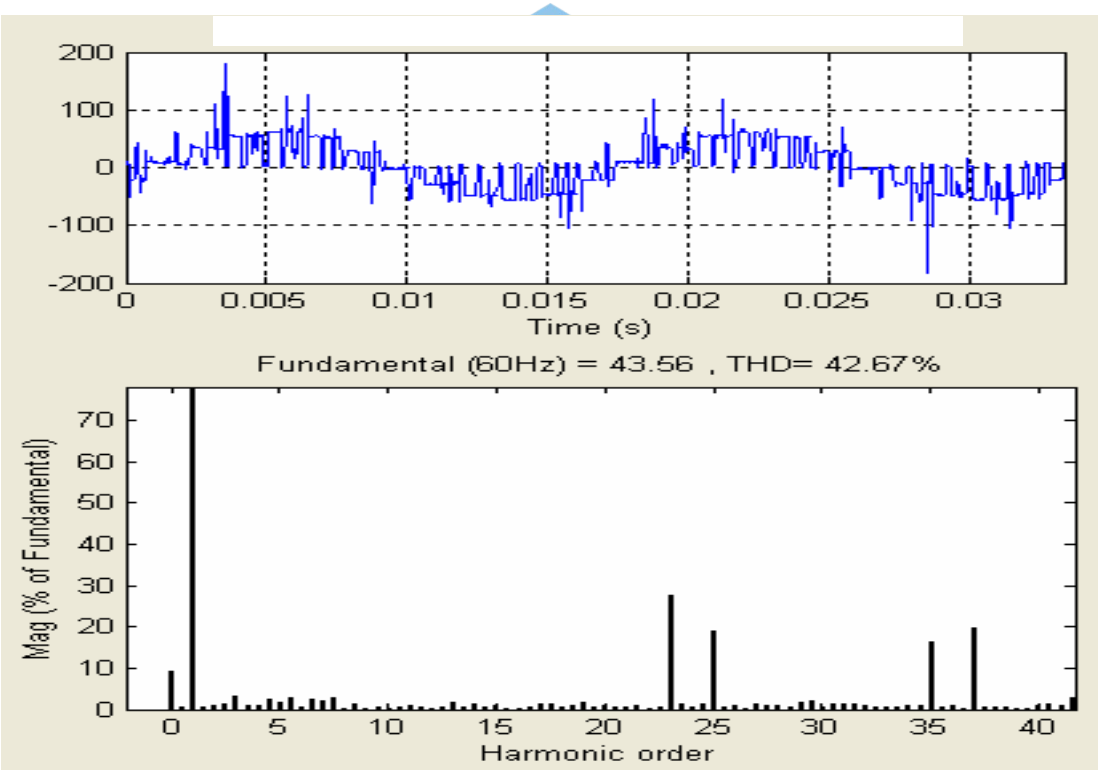

(b)

Fig.5-13 FFT analysis of the (a) simulated and (b) experimental line-to-line waveform of zig-zag output at modulation index of 0.5 and $\gamma_1 = 50^\circ$.

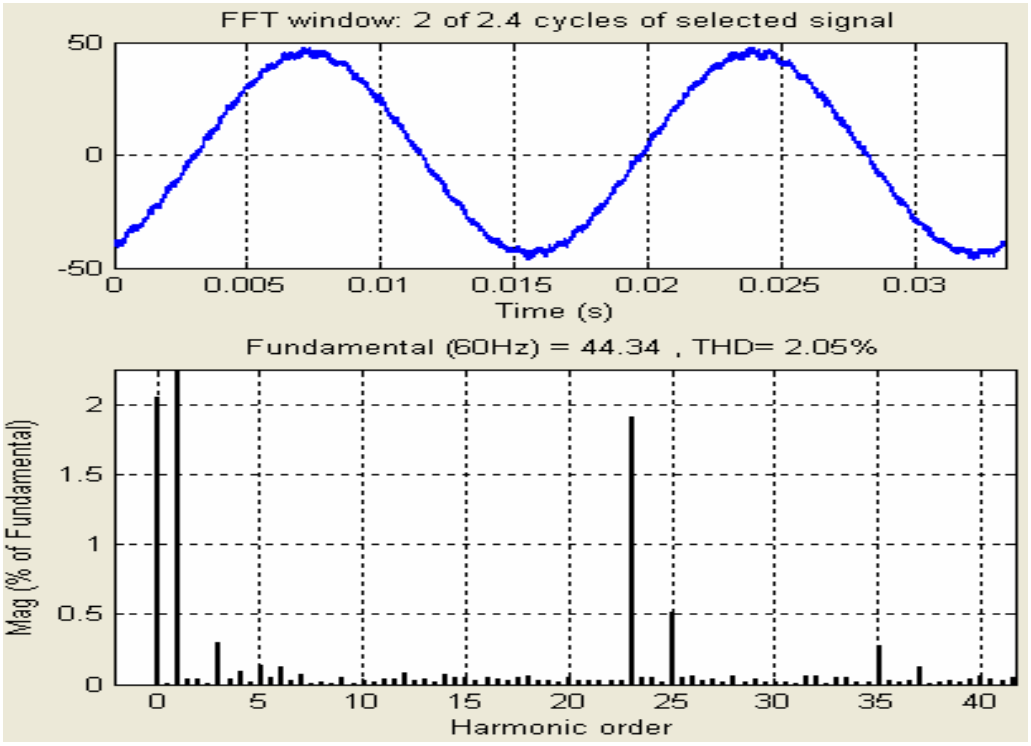

(a)

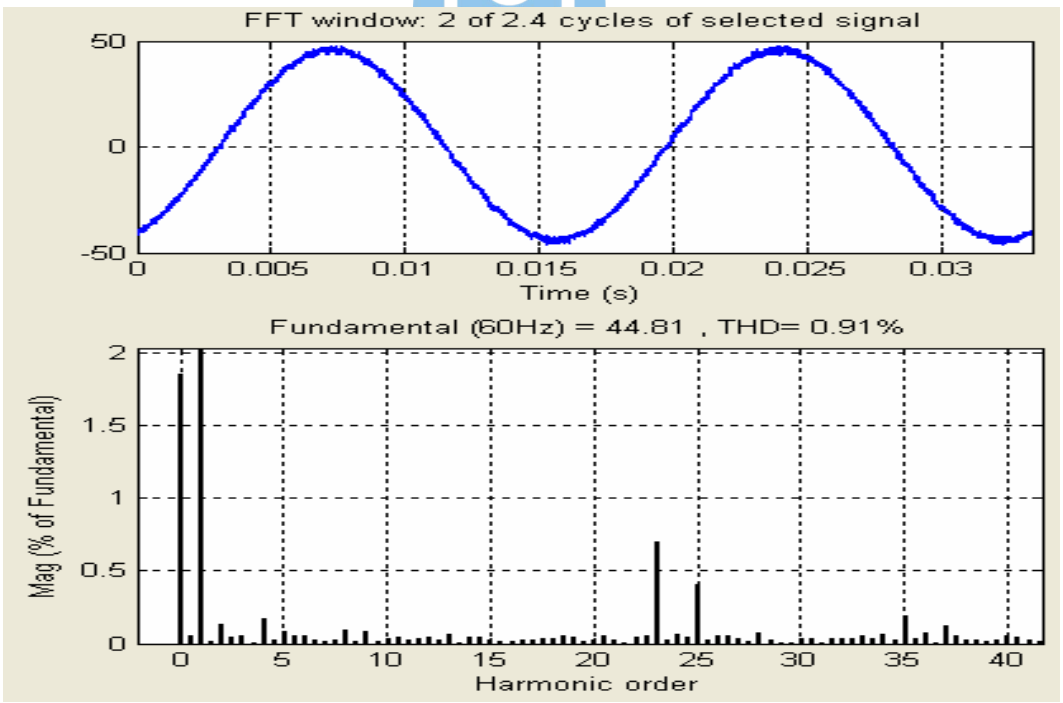

(b)

Fig.5-14 FFT analysis of the experimental line-to-line waveform of filter output at modulation index of 0.5 and (a) $\gamma_1 = 0^\circ$, (b) $\gamma_1 = 50^\circ$.

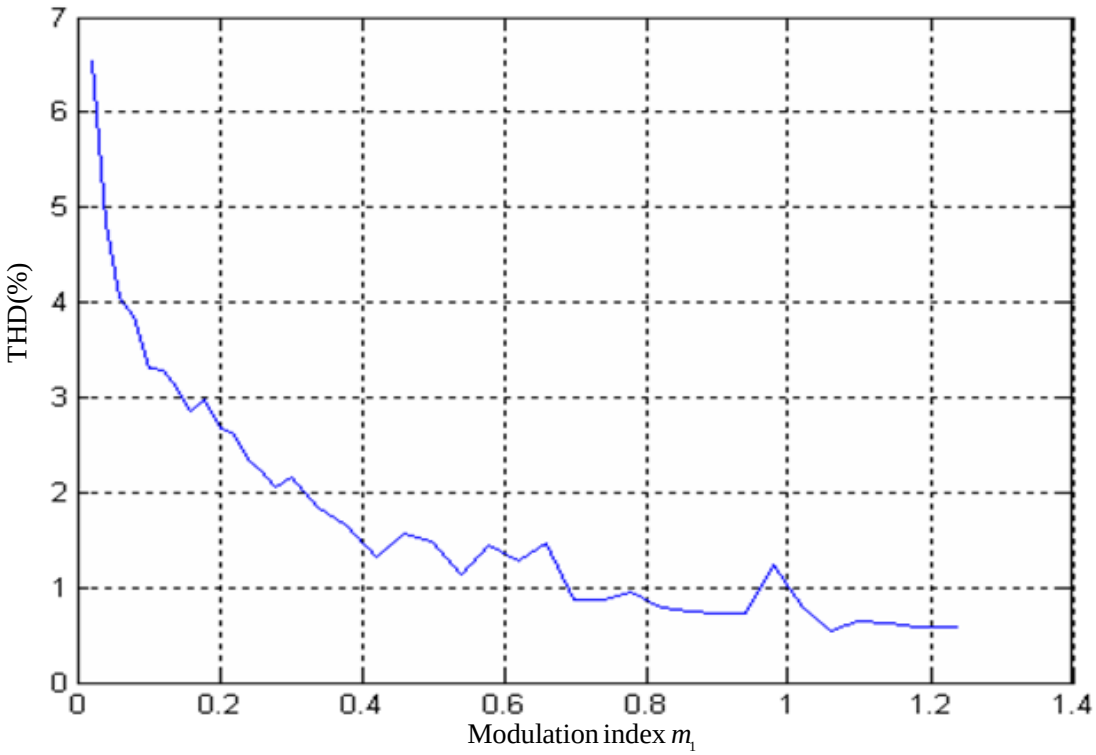

Fig. 5-15 The total harmonic distortion of the filter output line-to-line voltage of Route B from modulation index of 0.02 to 1.24.

Chapter 6 Conclusion

This thesis proposes a voltage source inverter (VSI) system cooperated with zig-zag connected transformers using selective harmonic elimination (SHE) technique. Selective harmonic elimination strategy is different from traditional pulse width modulation (PWM) strategy, which benefits lower switching frequency and directly controlling specific harmonics. The strategy is to control the fundamental, eliminate the 11-th and 13-th harmonics and minimize the 23-th and 25-th harmonics through a three-notch SHE switch signals. The harmonic orders other than $12n \pm 1$ are trapped in the secondary windings of the zig-zag connected transformers connected to the inverters. The full-range solutions, the modulation index from 0.02 to 1.20 and fundamental phases γ_1 from 0 to 360 degrees, are obtained by Newton-Raphson method. The most appropriate phases γ_1, which provides acceptable lower RSS (root sum square) of the 23-th and 25-th harmonics and smoother profile over the whole range of modulation index, are determined for real-time control.

Because the zig-zag connected transformers have the character of trapping the $12n \pm 1$ harmonics in the secondary windings, eliminating more harmonics other than $12n \pm 1$ harmonics gets lower THD of the output waveforms. Therefore, the future researches can focus on eliminating 11-th, 13-th, 23-th and 25-th harmonics, and reducing the 35-th and 37-th harmonics by shifting the fundamental phase to get better outputs. The higher level of the inverter output can also decrease the THD. On the other hand, Newton's method is not the only approach to solve

this nonlinear equation set. The other method such as genetic algorithm[28] could probably find the better solutions that Newton's method can't do. The optimized solutions might be found if the operation time is long enough when executing the genetic algorithm.

References

[1] N. Mohan, T. M. Undeland, and W. P. Robbins, “Power Electronics：Converters, Applications, and Design,” *New York：Wiley*, 3rd ed., 1995.

[2] S. A. Saleh, and M. A. Rahman, ‘‘Development and Experimental Testing of a Single-Phase B-Spline-Based SPWM Inverter,’’ *IEEE International Symposium on Industrial Electronics*, vol. 2, pp. 815-819, 2006.

[3] Y. Yuan, G. Yong, and L. Nan, ‘‘Design of three-phase SPWM signal generation system based on soft-switch technology,’’ *International Conference on Electronic Measurement and Instruments*, pp. 937-941, 2007.

[4] L. Jian, Z. Zhe, Y. Xianggen, and W. Minghao, ‘‘FPGA Implementation of a Multi-Level SPWM for Three-Level NPC Inverter,’’ *Proceedings of International Conference on Power Engineering*, vol. 1, pp. 175-179, 2006.

[5] J. Huang, R. Xiong, Z. Wang, W. Zuo, Y. Zhou, and H. Shi, ‘‘A Novel SPWM Control Strategy to Reduce Common-mode Voltage in Three-phase Four-leg Inverters,’’ *Proceedings of International Conference on Electrical Machines and Systems*, pp. 1526-1530, 2008.

[6] P. T. Cheng, and D. M. Divan, ‘‘Control of Quarter-wave Inverters in High-power Hybrid Active Filter Systems,’’ *IEEE Transactions on Industry Applications*, vol. 34, pp. 458-472, 1998.

[7] G. Poddar, and M. K. Sahu, ‘‘Natural Harmonic Elimination of Square-Wave Inverter for Medium-Voltage Application,’’ *IEEE Transactions on Power Electronics*, vol. 24, pp. 1182-1188, 2009.

[8] J. R. Espinoza, J. I. Guzmán, L. A. Morán, and R. P. Burgos, ‘‘Selective Harmonic Elimination and Current/Voltage Control in Current/Voltage-Source Topologies: A Unified Approach,’’ *IEEE Transactions on Industrial Electronics*, vol. 48, pp. 71-81, 2001.

[9] L. Xu, and V. G. Agelidis, ‘‘A VSC Transmission System Using Flying Capacitor Multilevel Converters and Selective Harmonic Elimination PWM Control,’’ *Proceedings of International Conference on Power Engineering*, vol. 2, pp. 1176-1181, 2005.

[10] S. A. Dahidah, and V. G. Agelidis, ‘‘Selective Harmonic Elimination PWM Control for Cascaded Multilevel Voltage Source Converters: A Generalized Formula,’’ *IEEE Transactions on Power Electronics*, vol. 23, pp. 1620-1630, 2008.

[11] Q. Liang, Z. Hui, L. Kaipei, and Q. Liu, ‘‘An Improved Modulation of the Selective Harmonic Elimination Controlling,’’

Proceedings of International Conference on Power System Technology, pp. 1-5, 2006.

[12] J. Sun, S. Beineke, and H. Grotstollen, ‘‘Optimal PWM Based on Real-Time Solution of Harmonic Elimination Equations,’’ *IEEE Transactions on Power Electronics*, vol. 11, pp. 612-62, 1996.

[13] S. R. Bowes, S. Grewal, and D. Holliday, ‘‘Single-phase Three-level Regular-sampled Selective Harmonic Elimination PWM,’’ *IEE Proceedings on Electric Power Applications*, vol. 148, pp. 155-161, 2001.

[14] A. I. Maswood, ‘‘PWM SHE Switching Algorithm for Voltage Source Inverter,’’ *Proceedings of International Conference on Power Electronics, Drives and Energy Systems*, pp. 1-4, 2006.

[15] C. Zheng, B. Zhang, and D. Qiu, ‘‘Solving Switching Angles for the Inverter's Selected Harmonic Elimination Technique with Walsh Function,’’ *Proceedings of International Conference on Electrical Machines and Systems*, vol. 2, pp. 1366-1370, 2005.

[16] N. A. Azli, and A. H. Yatim, ‘‘Curve Fitting Technique for Optimal Pulse Width Modulation (PWM) Online Control of a Voltage Source Inverter (VSI),’’ *TENCON*, vol. 1, pp. 419-422, 2000.

[17] J. R. Wells, B. M. Nee, P. L. Chapman, and P. T. Krein, ‘‘Selective Harmonic Control: A General Problem Formulation and Selected Solutions,’’ *IEEE Transactions on Power Electronics*, vol. 20, pp. 1337-1345, 2005.

[18] H. Huang, H. Shiyan, and D. Czarkowski, “Harmonic Elimination for Constrained Optimal PWM,” *IEEE on Industrial Electronics Society Conference Record*, vol. 3, pp. 2702-2705, 2004.

[19] J. R. Espinoza, G. Joos, J. I. Guzman, A. L. Moran, and R. P. Burgos, **“**Selective Harmonic Elimination and Current/Voltage Control in Current/Voltage-source Topologies: a Unified Approach,” *IEEE Transactions on Industrial Electronics*, vol. 48, no. 1, pp. 71-81, 2001.

[20] J. N. Chiasson, L. M. Tolbert, J. K. Mckenzie, and D. Zhong, “A Unified Approach to Solving the Harmonic Elimination Equations in Multilevel Converters,” *IEEE Transactions on Power Electronics*, vol. 19, no. 2, pp. 478-490, 2004.

[21] A. Bhadkamkar, A. Bendre, R. Schneider, W. Kranz, and D. Divan, ‘‘Application of Zig-zag Transformers in a Three-wire Three-phase Dynamic Sag Corrector System,’’ *Power Electronics Specialist Conference*, vol. 3, pp. 1260-1265, 2003.

[22] H. L. Jou, J. C. Wu, K. D. Wu, W. J. Chiang, and Y. H. Chen, ‘‘Analysis of Zig-zag Transformer Applying In the Three-phase Four-wire Distribution Power System,’’ *IEEE Transactions on*

Power Delivery, vol. 20, pp.1168-1173, 2005.

[23] 巫昇峰, “基於曲折繞接線變壓器利用特定諧波消除之三階層反流器研製,” 國立台灣科技大學電機工程系碩士學位論文, 民國九十六年

[24] C. R. Penney, ‘‘Linear Algebra : Ideas and Applications,’’ *Hoboken, N. J. : Wiley-Interscience*, c2004.

[25] 張棟樑, “以變壓器曲折繞法及特定諧波消除為基礎之三相變流器諧波消除,” 國立台灣科技大學電機工程系碩士學位論文, 民國九十三年

[26] W. Zhang, and Y. Sun, ‘‘Optimization of Output Voltage Waveform of Selective Harmonic Elimination Inverter,’’ *Proceedings of International Conference on Power System Technology*, pp.1-4, 2006.

[27] V. Laurene, ‘‘Applied Numerical Analysis Using MATLAB,’’ *Upper Saddle River, NJ: Pearson Education International*, 2008.

[28] M.A. Marra, B.L.Walcott, “Stability and Optimality in Genetic Algorithm Controllers,” *IEEE International Symposium on Intelligent Control*, pp. 492-496, 1996.

國立臺灣科技大學博碩士論文授權書

(本授權書裝訂於紙本論文內)

本授權書所授權之論文為劉彥中〔M9607236〕在國立臺灣科技大學電機工程系 97 學年度第 2 學期取得碩士學位之論文。

論文題目：　基於曲折繞接式變壓器利用特定諧波消除之多階層反流器研製
指導教授：　楊宗銘

茲同意將授權人擁有著作權之上列論文全文〔含摘要〕，依下述授權範圍，以非專屬、無償授權本校圖書館及國家圖書館，不限地域、時間與次數，以紙本、微縮、光碟或其他數位化方式將上列論文重製典藏，並提供讀者基於個人非營利性質之線上檢索書目、館內閱覽、或複印。

授權人　劉彥中　楊宗銘　楊宗銘

簽章
(請親筆正楷簽名)　劉彥中

備註：

1. 授權人不因本授權而喪失上述著作之著作權。
2. 本授權書請授權人簽章後，裝訂於紙本論文內。

中　華　民　國　98　年　7　月　9　日